SUPERSYMMETRY SEARCH VIA EXCESS OF TOP QUARKS EVENTS

Mr. Nattawit Chaiworawitsakul

A Thesis Submitted in Partial Fulfillment of the Requirements

for the Degree of Master of Science Program in Physics

Department of Physics

Faculty of Science

Chulalongkorn University

Academic Year 2013

การค้นหาสมมาตรยวดยิ่งผ่านเหตุการณ์ที่มีท็อปควาร์กส่วนเกิน

นายณัฐวิทย์ ไชยวรวิทย์สกุล

Thesis Title   SUPERSYMMETRY SEARCH VIA EXCESS OF TOP
                 QUARKS EVENTS

By   Mr. Nattawit Chaiworawitsakul

Field of Study   Physics

Thesis Advisor   Assistant Professor Burin Asavapibhop, Ph.D.

Accepted by the Faculty of Science, Chulalongkorn University in Partial Fulfillment of the Requirements for the Master's Degree

.... Dean of the Faculty of Science
(Professor Supot Hannongbua, Dr.rer.nat.)

THESIS COMMITTEE

.... Chairman
(Assistant Professor Auttakit Chatrabhuti, Ph.D.)

.... Thesis Advisor
(Assistant Professor Burin Asavapibhop, Ph.D.)

.... Examiner
(Assistant Professor Surachate Limkumnerd, Ph.D.)

.... External Examiner
(Assistant Professor Chinorat Kobdaj, Ph.D.)

ณัฐวิทย์ ไชยวรวิทย์สกุล : การค้นหาสมมาตรยวดยิ่งผ่านเหตุการณ์ที่มีท็อปควาร์กส่วนเกิน. (SUPERSYMMETRY SEARCH VIA EXCESS OF TOP QUARKS EVENTS) อ.ที่ปรึกษาวิทยานิพนธ์หลัก : ผศ.ดร.บุรินทร์ อัศวพิภพ, 57 หน้า.

ทฤษฎีสมมาตรยวดยิ่งเป็นหนึ่งในตัวเลือกสำหรับภาคขยายของทฤษฎีแบบจำลองมาตรฐานของฟิสิกส์อนุภาค ทฤษฎีนี้สามารถแก้ไขปัญหาหลาย ๆ อย่างในทฤษฎีแบบจำลองมาตรฐานได้ ทฤษฎีนี้ทำนายว่าทุก ๆ อนุภาคมูลฐานในทฤษฎีแบบจำลองมาตรฐานจะมีคู่ของอนุภาคนั้นที่มีสปินต่างออกไป 1/2 โดยที่อนุภาคเหล่านี้เป็นอนุภาคที่ไม่เสถียรและสามารถสลายตัวกลับมาเป็นอนุภาคในแบบจำลองมาตรฐานได้ วิทยานิพนธ์นี้ทำการศึกษาวิธีการคัดเลือกสัญญาณจากทฤษฎีสมมาตรยวดยิ่งที่จุดทดสอบแอลเอ็มเก้าโดยศึกษาสมบัติต่าง ๆ ของตัวแปรที่มีต่อสัญญาณที่ศึกษาและเหตุการณ์พื้นหลังต่าง ๆ และพัฒนาวิธีการคัดเลือกต่าง ๆ เพื่อให้มีอัตราส่วนระหว่างสัญญาณที่ต้องการต่อเหตุการณ์พื้นหลังสูงที่สุด เหตุการณ์พื้นหลังที่ศึกษาในวิทยานิพนธ์นี้ประกอบด้วยเหตุการณ์ของท็อปควาร์ก เหตุการณ์ที่เกิดขึ้นจากกระบวนการทางคิวซีดี และเหตุการณ์ที่เกิดขึ้นจากกระบวนการทางอิเล็กโตรวีก เหตุการณ์ทั้งหมดถูกจำลองขึ้นโดยวิธีมอนติคาร์โล ปริมาณเหตุการทั้งหมดได้ถูกปรับให้อยู่ในระดับที่เทียบเท่ากับค่าลูมินอซิตี้สะสม 183 ต่อพิโกบาร์น

ภาควิชา ฟิสิกส์ .... ลายมือชื่อนิสิต ....

สาขาวิชา ฟิสิกส์ .... ลายมือชื่อ อ.ที่ปรึกษาวิทยานิพนธ์หลัก ....

ปีการศึกษา 2556 ....

5372244323 : MAJOR PHYSICS
KEYWORDS : SUPERSYMMETRY / CMS / LHC / CERN

NATTAWIT CHAIWORAWITSAKUL : SUPERSYMMETRY SEARCH
VIA EXCESS OF TOP QUARKS EVENTS. ADVISOR : ASST. PROF.
BURIN ASAVAPIBHOP, Ph.D., 57 pp.

Supersymmetry (SUSY) is an extension candidate for the Standard Model. It offers solutions to many problems in the Standard Model. It is proposed that there is a new copy of Standard Model particles with spin differ by $1/2$. These particles are unstable and very massive, and will decay into Standard Model particles. In this thesis, the selection cuts for SUSY signal at LM9 test point has been developed. Various variables are studied for their characteristic against signal and different backgrounds. The selection has been optimized to give a better signal to backgrounds ratio. The backgrounds used in the thesis consist of top events, QCD events, and Electroweak events. All samples are simulated by Monte Carlo simulation and normalized to 183 pb^{-1} integrated luminosity.

Department : Physics .... Student's Signature ....

Field of Study : Physics .... Advisor's Signature ....

Academic Year : 2013 ....

Acknowledgements

First and foremost, I am very delighted to express my gratitude to Asst. Prof. Burin Asavapibhop, my advisor, for his guidance, patience, and everything he has done for me. I wouldn't have come this far without his supports. I am very thankful to Dr. Norraphat Srimanobhas and Dr. Emanuele Simili for every help and advise on the CMS software and ROOT framework.

I would like to thank Asst. Prof. Auttakit Chatrabhuti, Asst. Prof. Surachate Limkumnerd, and Asst. Prof. Chinorat Kobdaj for devoting their valuable time to be my thesis examiners.

I would like to thank my family. Whatever I want to do, they are always there to support me and never tell me I can't do that. I also thank Chalinee Thanasubsombat for cheering me and pushing me to finish this thesis. Lastly, I would like to thank all of my friends, especially the RabbitJam group, for all the joyful time that I have with them.

Contents

List of Tables

List of Figures

Figure   **page**

CHAPTER I

Introduction

"What is matter made up of?" is what we, humans, have asked since the ancient times. The theory of atomism was developed for the first time by Leocippus, the Greek philosopher, and his student in 5th century BC. According to this theory, all matters are composed of tiny indivisible particles called "atoms". But it has to wait until 19th century, that the evidence of the existence of atom has been observed for the first time. The word "atom" was used again by John Dalton as a unique particle that represents each type of elements. These different atoms combined into different molecules and give a wide range of properties. These atoms were believed to be unbreakable particles until the discovery of electron in 1897 and nucleus in 1909. As a results of these observations, the idea of atom had been changed from an unbreakable particle to a planetary model where electrons circulate around a nucleus. Then in 1917, the nucleus was, again, found out that it is not an indivisible particle, but consists of smaller particles called proton and neutron. Since then, the nuclear physics has progressed with an amazing speed. Many new particles were observed, many new accelerators and colliders were built. The theory of elementary particles was fabricated by many theorists and confirmed by many experiments all over the world. Every piece of the theory has been put together and combined into a single model called "the Standard Model of Particle Physics." The Standard Model has been proved and measured very precisely. It can explain the behaviour of almost all particles that we know today. But still, the Standard Model is far from a perfect theory. There are many problems that need to be solved, such as hierarchy problem, dark matter, and dark energy. The Standard Model still doesn't include gravity in the theory yet, this is very essential

because gravity plays a crucial part in the cosmic scale. In order to investigate physics beyond the Standard Model, we require a more powerful collider such as the Large Hadron Collider (LHC) at CERN. The LHC is the most powerful accelerator at the moment. It has been running for 3 years since 2010 and entered the first upgrade period in 2013. With the outstanding performance of LHC, the Higgs bosons, as the last piece of the Standard Model, was discovered on July 4, 2012 by the two experiments operated at LHC. The LHC will resume its operation in 2015 with almost double energy compared to the first run. It is very promising that a lot of discoveries will be made with this huge amount of energy increase.

The analysis in this thesis will focus on the searching for the excess of hadronic top that decays from supersymmetric particles using the Monte Carlo sample from the CMS collaboration. The characteristic of four cut variables for signal and different backgrounds are investigated: H_{T}, $E_{\mathrm{T}}^{\mathrm{miss}}$, $\Delta\phi_N^{\mathrm{min}}$, and number of b-jets. The initial cuts are applied to these variables and are inspected for the efficiency of cut on each variable. Then, the selection cuts are improved by maximizing the Q factor to give the best performance in extracting signal from various backgrounds. This thesis is organized as follows. We begin in Chapter 2 with the review of the Standard Model of particle physics as we know today. We continue with the problems in Standard Model and overview of supersymmetry model. In Chapter 3, the design and operation performance of the LHC are given, along with the detailed configurations of the Compact Muon Solenoid detector (CMS). Chapter 4 explains the brief review of the algorithm used in the CMS detector to reconstruct the measured electric signal into physics object candidates. Chapter 5 shows the detail of the samples, analysis and the results of this thesis. And lastly, Chapter 6 which concludes everything.

CHAPTER II

The Standard Model and Supersymmetry

2.1 The Standard Model

The Standard Model of particle physics is a very powerful theory in describing the interactions of subatomic particles. It can explain a variety of phenomena to the very precise digit [1], and has also predicted many particles that have yet to be found at that time. From the Standard Model's aspect, matters are built up from various elementary particles which can be classified into three classes, lepton quark and gauge boson.

2.1.1 Lepton

There are six types (or flavours) of lepton forming three generations. Electron, muon, and tau have spin $\frac{1}{2}$ and have -1 elementary charge (roughly $1.602176565 \times 10^{-19}$ coulomb), while their corresponding neutrinos have the same spin but carry no charge. Tau which is the heaviest lepton(≈ 1.777 GeV) will immediately decay into electron, muon ,or quarks and one or two neutrinos. Muon has mass of 105.6 MeV and mean lifetime of 2.197×10^{-6} s which will decay into electron, electron antineutrino, and muon neutrino. Lastly, electron with mass of 0.511 MeV is a stable particle. Neutrino is a theoretically massless particle, but the results from recent experiments [3, 4] indicate that neutrino is not a completely
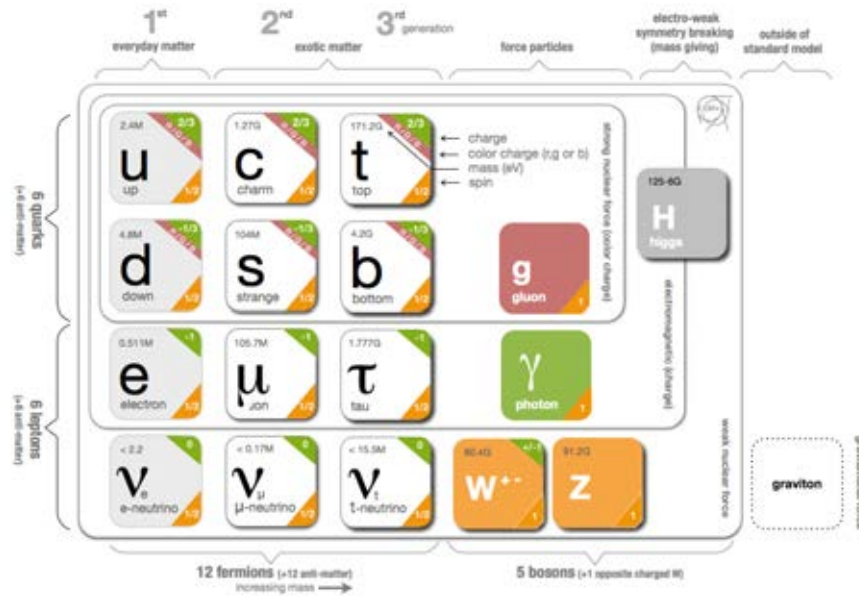
Figure 2.1: List of Standard Model's elementary particles [2].

massless particle but in fact has a very tiny mass. This is one of the problems that cannot be explained yet. Additionally, leptons also have another property called lepton numbers. Each generation has its own lepton numbers (electronic number, muonic number and tauonic number) and these number must be conserved in every observed interaction.

2.1.2 Quark

Quark has six flavours and three generations, namely up and down, charm and strange, top and bottom. Each has spin $\frac{1}{2}$ since they are also fermions. As for charge, the up-like quark (up, charm and top) have $+\frac{2}{3}e$ while the down-like quark (down, strange and bottom) have $-\frac{1}{3}e$. Quarks have a very wide mass spectrum from up and down quark which carry mass of only 2.3 and 4.8 MeV respectively, strange with 95 MeV mass, and range up to the GeV scale with 1.27 GeV charm quark and 4.18 GeV bottom quark ($\overline{MS}$) [5]. Top quark which is the heaviest quark and also the heaviest particle in the Standard Model weighs up to 173.5 GeV, which is as heavy as a gold atom.

Furthermore, quark has another quantum property called "color charge,"

which contributes to the strong interaction between particles. These color charges are not the actual color that we normally see with own eyes, but just an analogy between real colors and these charges' behaviour. Color charges have three different types i.e. red, green and blue taken from three primary colors. Just like electric charge, color charge can also have a negative value of charge that is antired, antigreen, or antiblue. Every particle that carries color charge will be subjected to a phenomenon called color confinement, which states that any free particle cannot have a color charge. In other words, every particles that carry color charge must bind themselves with other particles into a new colorless composite particle [6]. In a particle accelerator where high energy quarks are created constantly and act like free-particles, the energy from these quarks will convert into a new quark-antiquark pair resulting in the lower energy of the original quarks. This process is called "hadronization" and will continue until all quarks have their energies low enough to create a bound state with each other leaving only showers of colorless hadrons. These showers will be reconstructed as "jets" in an analysis and used to represent quarks created in the collision.

Unlike the other quarks, top has an extremely short lifetime $\tau_t \approx 5 \times 10^{-25}$s, which is one order of magnitude smaller than the hadronization time $\tau_{had} \approx 1/\Lambda_{QCD} \approx 3 \times 10^{-24}$ s [7]. This mean that top cannot form any top-meson $t\bar{q}$ or top-baryon tqq', but will decay before the hadronization process even begin. Generally, top will decay into W boson and any down-like quark. The most probable channel is $t \rightarrow W + b$ with branching ratio $\Gamma(Wb)/\Gamma(Wq(q = b, s, d)) = 0.91 \pm 0.04$. Furthermore, top quark can sometimes decay into an exotic decay channel like $t \rightarrow \gamma + q(q = u, c)$ or $t \rightarrow Z + q(q = u, c)$ with a very small probability.

2.1.3 Gauge boson

Gauge boson is a bosonic particle with spin 1. Unlike the quark and lepton, gauge boson is not a particle that made up matter, but instead, it mediates the interaction between matters. In particle physics, force or interaction is in fact just a result from exchanging gauge bosons between matter particles, and each

gauge boson will correspond to each type of fundamental interaction. The first gauge boson is photon, labeled as γ, which is a force carrier for electromagnetic interaction. It is a massless particle which is widely known as a light particle and it can interact with every particle that carries either positive or negative electric charge.

The next interaction is the weak interaction which is responsible for the decay process in nuclear and particle physics. Its corresponding carrier particles are W and Z bosons with masses of 80.4 and 91.2 GeV, respectively. W bosons can have either positive or negative elementary electric charge (W^+ or W^-) while Z boson has zero charge. Since they are so massive, the range for weak interaction become very short and W and Z bosons will decay immediately after the creation. Z boson's decay mode can be divided generally into 3 channels, the leptonic channel where it decays into either electron muon or tau and its antiparticle, the invisible channel where it decays into neutrino and antineutrino which can't be detected by any detectors, and lastly, the hadronic channel where it decays into any quark and antiquark resulting showers of hadrons detected in detectors. As for W^+ boson, it can decay into only 2 channels, the leptonic channel and hadronic channel. In the leptonic channel, W^+ boson will decay into a positive lepton and its neutrino, while in hadronic channel, it will decay into up or charm and any anti-down-like quark. The decay channels of W^- are exactly the same as W^+'s except that every particles become their antiparticles. The detailed decay channel are shown in table 2.1

W^+ **DECAYS MODES**	Fraction (Γ_i/Γ)	Z **DECAY MODES**	Fraction (Γ_i/Γ)
$l^+\nu$	$(10.80 \pm 0.01)\%$	l^+l^-	$(3.3658 \pm 0.0023)\%$
$e^+\nu$	$(10.75 \pm 0.13)\%$	e^+e^-	$(3.363 \pm 0.004)\%$
$\mu^+\nu$	$(10.57 \pm 0.15)\%$	$\mu^+\mu^-$	$(3.366 \pm 0.007)\%$
$\tau^+\nu$	$(11.25 \pm 0.20)\%$	$\tau^+\tau^-$	$(3.370 \pm 0.008)\%$
$hadrons$	$(67.60 \pm 0.27)\%$	$invisible$	$(20.00 \pm 0.06)\%$
		$hadrons$	$(69.91 \pm 0.06)\%$

Table 2.1: Decay modes of W^+ and Z bosons.

The last type of gauge bosons is gluon. It represents the strong nuclear interaction which holds quarks together into a hadron, and is responsible for the forming of a nucleus. It is a massless particle with no electric charge, but carries both color charge and anticolor charge at the same time. There are totally eight types of gluon which are independent superposition color states as listed below [8].

$$
\begin{array}{ll}
\left(r\bar{b} + b\bar{r}\right)/\sqrt{2} & -i\left(r\bar{b} - b\bar{r}\right)/\sqrt{2} \\
\left(r\bar{g} + g\bar{r}\right)/\sqrt{2} & -i\left(r\bar{g} - g\bar{r}\right)/\sqrt{2} \\
\left(b\bar{g} + g\bar{b}\right)/\sqrt{2} & -i\left(b\bar{g} - g\bar{b}\right)/\sqrt{2} \\
\left(r\bar{r} + b\bar{b}\right)/\sqrt{2} & \left(r\bar{r} + b\bar{b} - 2g\bar{g}\right)/\sqrt{6}
\end{array}
\tag{2.1}
$$

And because gluons carry color charges, they can interact with themselves and also are subjected to the color confinement and create jets as they fly out from the interaction point.

2.1.4 Higgs boson

Higgs boson is the last piece of puzzle to complete the Standard Model. It gives an origin to the mass of every particle in the Standard Model. Higgs boson has been discovered on 4 July 2012 as a new unknown boson by both ATLAS and CMS[9, 10], and has been confirmed as a Higgs boson later on 14 March 2013. Higgs boson has, theoretically, spin zero and no charge. The mass of Higgs boson is not predicted directly from the theory but from the most recent measurement by CMS and ATLAS experiments, Higgs has mass 125.3 [10] and 126.0 [11] GeV respectively. The mean lifetime τ for Higgs boson at 126 GeV is predicted to be 1.56×10^{-22} s [12].

Roughly speaking, Higgs boson can decay into any pair of massive particles, since those particles must interact with Higgs field to gain mass. The first possibility is Higgs decays into fermion-antifermion pair. Due to the fact that mass of fermions depends directly on the strength of the interaction between fermions and Higgs field, this makes Higgs tends to decay into heavier fermions than the lighter
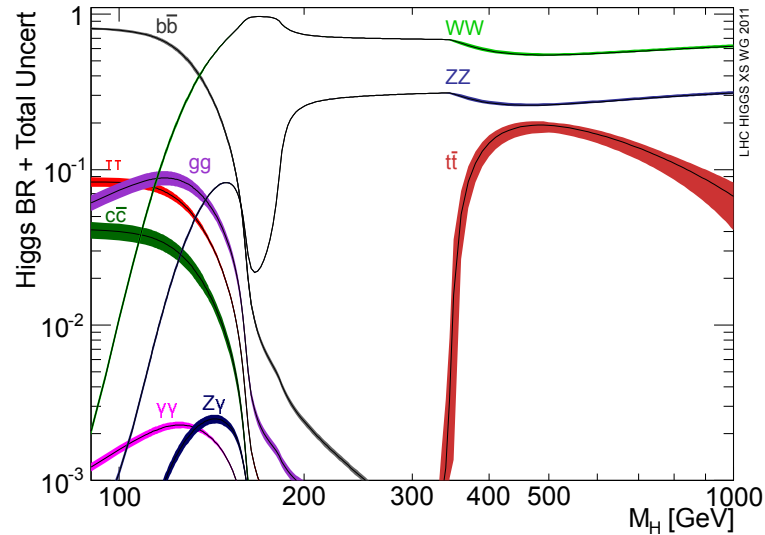
Figure 2.2: Higgs branching ratios and their uncertainties for the full mass range [12].

ones. The best candidate in this case is top quark which is the heaviest fermion in the Standard Model. But this channel become impossible because Higgs has mass only 126 GeV, far lower than mass of top-antitop pair. The most common decay for Higgs has then become bottom-antibottom pair with probability of 56.1%. The next probable decay channel for Higgs decaying into fermions pair is tau-antitau and charm-anticharm with the chance of 6.15% and 2.83% respectively. Another possibility is that Higgs splits into a pair of massive gauge bosons like WW with 23.1% chance or ZZ with only 2.89%. Higgs can also decay into massless particles but required a loop of intermediate virtual heavy particles like top or W bosons. The notable channels for this type of decay are Higgs decaying into a pair of gluons which happens 8.48% of the time and Higgs decays into a pair of photons with only 0.23% chance. The latter channel is very important because it gives a very pure signal and high resolution of energy and momentum for Higgs reconstruction.

Figure 2.3: One loop quantum correction to the Higgs squared mass parameter m_H^2, due to (a) a Dirac fermion f, and (b) a scalar S.

2.2 Supersymmetry

Supersymmetry is one of the main candidates as an extension to the Standard Model [13]. One of the motivations for the supersymmetry is the "hierarchy problem" that arises from the calculation of Higgs mass in the Standard Model. For any fermion f, we can have the Higgs mass correction term from loop diagram as shown in Fig 2.3 (a). If the Higgs field couples to f with a term $-\lambda_f H \bar{f} f$, then the loop will yield correction:

$$\Delta m_H^2 = -\frac{|\lambda_f|^2}{8\pi^2} \Lambda_{\text{UV}}^2 + \dots. \tag{2.2}$$

where Λ_{UV} is an ultraviolet momentum cutoff which can be interpreted as a point where new physics occur. The ellipsis represent an additional terms which grows at most logarithmically with Λ_{UV}. The cutoff can be any value range from the electroweak scale ($\sim 100\,\text{GeV}$) to Plank scale ($\sim 10^{34}\,\text{GeV}$). But we have already discovered Higgs bosons with 125 GeV mass. If the correction term is really in the Plank scale, then the higgs bare mass must also be equally high and have almost exactly the same value down to 32 digits. Of course, it is not a problem at all, the universe can work that way. But we have the belief that our elegant universe should be explained by a simpler theory than a very fine-tuning of two different variables. We can also choose the cutoff value that is not too large. But then again, we will need a new physics and that might give rise to another massive particle that contributes more to the correction of Higgs mass. Or it could be that Higgs boson is not a fundamental particle, but rather a composite particle. These are options that have been investigated by many theorists all over the world. But

another option that is more widely believed is that there is some cancellation in the correction terms that remove the ultraviolet part completely. Considering a new complex scalar particle S with mass m_S that couples to the Higgs field with a Lagrangian term $-\lambda_S|H|^2|S|^2$. Then the Feynman diagram in Fig 2.3 (b) gives a correction:

$$\Delta m_H^2 = \frac{\lambda_S}{16\pi^2}\left[\Lambda_{\text{UV}}^2 - 2m_S^2\ln(\Lambda_{\text{UV}}/m_S) + \dots\right]. \tag{2.3}$$

Notice that the sign of correction term is opposite to that of fermion. If each quark and lepton in the Standard Model has two corresponding complex scalar bosons with $\lambda_S = |\lambda_f|^2$, all of the ultraviolet correction will be cancelled out completely. This can be possible if we introduce a new symmetry between fermions and bosons.

Supersymmetry has proposed a new operator Q that turns a bosonic state into a fermionic state, and vice versa.

$$Q|\text{Boson}\rangle = |\text{Fermion}\rangle, \qquad\qquad Q|\text{Fermion}\rangle = |\text{Boson}\rangle \tag{2.4}$$

The operator Q and its hermitian conjugate $Q^\dagger$ must satisfy the following anti-commutation and commutation relations

$$\{Q, Q^\dagger\} = P^\mu, \tag{2.5}$$

$$\{Q, Q\} = \{Q^\dagger, Q^\dagger\} = 0, \tag{2.6}$$

$$[P^\mu, Q] = [P^\mu, Q^\dagger] = 0, \tag{2.7}$$

where P^μ is the four momentum generator of spacetime translations. Supersymmetry also introduces the new particle state called "supermultiplet" which contains both bosonic and fermionic states, commonly known as "superpartner" of each other. The chiral supermultiplet contains two complex scalar fields and a single two-component Weyl fermion field, while the gauge supermultiplet contains two gauge boson fields and a two-component Weyl fermion field. Since Q commutes with P^μ, it must also commute with square-mass operator P^2 and resulting in the same mass for both fermion and boson. But the fact is we have never detected any of these superpartners even once, this indicates that superpartners of

Standard Model paritcle must have mass much heavier than the one from the Standard Model and the supersymmetry requires an unknown soft term that breaks the symmetry spontaneously.

In general, we can have as many as supermultiplets and operator Q as we want. But in order to reduce the complexity, only a minimal amount of supersymmetry required to extend the Standard Model is considered. This model is called Minimal Supersymmetric Standard model or MSSM. In this model, all Standard Model particles will have their superpartner with the same symbols but have an additional tilde over their heads. The superpartners of Standard Model fermion have spin-0, and have the same name as their partners with an additional 's' in front of their names, such as slepton ($\tilde{l}$), squark ($\tilde{q}$), or stop ($\tilde{t}$). The superpartners of gauge bosons are spin-$^1/_2$ fermions called "gauginos". Each individual gaugino is named gluino, wino, and bino corresponding to gluon, W boson, and B boson, respectively. Higgs, on the other hand, is very special since MSSM requires four Higgs bosons in the Standard Model, namely H_u^+ H_u^0 H_d^0 and H_d^- and their corresponding superpartners are $\tilde{H}_u^+$ $\tilde{H}_u^0$ $\tilde{H}_d^0$ and $\tilde{H}_d^-$. After the breaking of electroweak symmetry, colorless gauginos and Higgsinos will mix into four neutralinos ($\tilde{\chi}_1^0, \tilde{\chi}_2^0, \tilde{\chi}_3^0, \tilde{\chi}_4^0$) and two charginos ($\tilde{\chi}_1^\pm, \tilde{\chi}_2^\pm$). By convention, these label are arranged such that $m_{\tilde{\chi}_1^0} < m_{\tilde{\chi}_2^0} < m_{\tilde{\chi}_3^0} < m_{\tilde{\chi}_4^0}$ and $m_{\tilde{\chi}_1^\pm} < m_{\tilde{\chi}_2^\pm}$.

In MSSM, the lepton number and baryon number can be violated and allows many new decays to occur. The new decay channels cause some problems as it also allows proton to decays into meson and lepton with a rapid rate. This contradicts what we have observed in reality that proton is a very stable particle with lifetime longer than 10^{33} years as far as we know. This decay can be prevented by introducing a new conservation law called R-parity. It is defined for each particle as

$$P_R = (-1)^{3(B-L)+2s}. \tag{2.8}$$

Where B is the baryon number, L is the lepton number, and s is the spin of the particle. The product of P_R in every vertex must be +1. With this, the decay
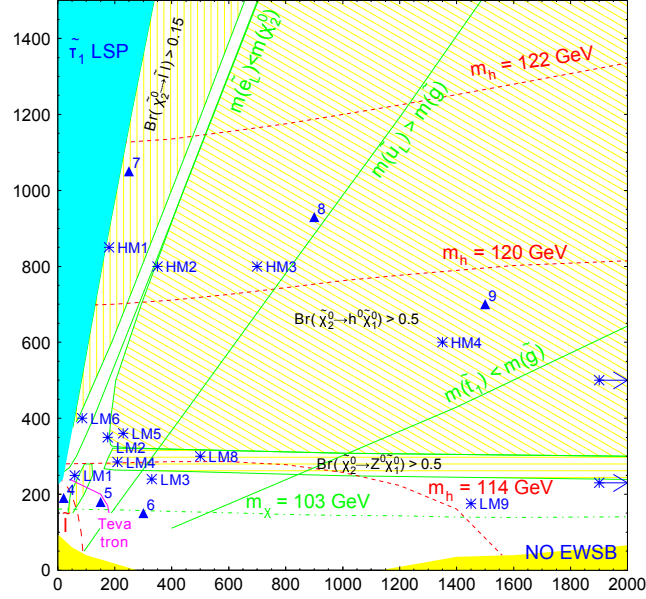
Figure 2.4: Position of test points in the m_0 versus $m_{1/2}$ plane. the lines in this plane correspond to the fixed value of $\tan\beta = 10$, $A_0 = 0$, and $\mu > 0$. All the test points are plotted using the stars as indicators.

process of protons has been prevented. This R-parity conservation also tells us that there should be an even number of supersymmetric particles in every vertex. This forces the decay process of massive superpartners to have at least one stable lightest supersymmetric particle (LSP) at the end of a decay chain. This particle will weakly interact with matter, escape the detector, and leave a huge amount of missing transverse momentum as a key signal for supersymmetry search. This particle can also be a candidate for the cold dark matter model.

The MSSM can be spontaneously broken in many ways. But the one that is most popular in phenomenological supersymmetry is the "minimal supergravity" or mSUGRA. After applying several more constraints, the huge amount of parameters in MSSM are reduced to only five free parameters which make the theory touchable from the experimental point of view. The five free parameters are listed below.

- m_0 : common mass of scalars

- $m_{1/2}$: common mass of gauginos and higgsinos

- A_0 : common trilinear coupling

- $\tan\beta$: ratio of Higgs vacuum expectation values

- $\text{sign}\,\mu$: μ is SUSY conserving Higgsino mass parameter

If we plot the plane m_0 versus $m_{1/2}$ with the fixed value of A_0, $\tan\beta$, and $\text{sign}\,\mu$, we can divide the plane into three regions. The first region is where gluinos are heavier than any squarks (the region above $m(\tilde{u}_L) > m(\tilde{g})$ line in Fig 2.4). The decay chains of sparticles are expected to be $g \to \tilde{q}\bar{q}$, $\tilde{q} \to q\chi$. Region 2 where some squarks are heavier than gluinos while others are lighter (the middle region in Fig 2.4). The heavy squark can decay into gluino and gluino can subsequently decay into the lighter squark: $\tilde{q}_L \to \tilde{g}q$, $\tilde{g} \to \tilde{b}\bar{b}$, $\tilde{b} \to b\chi$. The last region in the bottom of Fig 2.4 is where the gluinos are lighter than any squarks. Then squarks will decay into gluinos: $\tilde{q} \to \tilde{g}q$, $\tilde{g} \to q\bar{q}\chi$. The decay chain will continue until it reaches $\tilde{\chi}_1^0$ which is the lightest supersymmetric particle.

In CMS collaborations, a set of mSUGRA test point has been defined for various supersymmetry analyses [14]. The low mass (LM) points have been chosen to evaluate the sensitivity to SUSY signals in the early period of LHC operations, and some high mass (HM) points near the ultimate reach of the LHC were also included. The list of parameters for each test point is given in Table 2.2 and their positions in m_0-$m_{1/2}$ plane are shown in Fig 2.4 with blue stars. Each test point will have a different decay chain and branching ratio based on its parameters.

Point	m_0	$m_{1/2}$	$\tan\beta$	sign(μ)	A_0
LM1	60	250	10	+	0
LM2	185	350	35	+	0
LM3	330	240	20	+	0
LM4	210	285	10	+	0
LM5	230	360	10	+	0
LM6	85	400	10	+	0
LM7	3000	230	10	+	0
LM8	500	300	10	+	-300
LM9	1450	175	50	+	0
LM10	3000	500	10	+	0
HM1	180	850	10	+	0
HM2	350	800	35	+	0
HM3	700	800	10	+	0
HM4	1350	600	10	+	0

Table 2.2: mSUGRA parameter values for the test points. Masses are given in units of GeV.

CHAPTER III

Accelerator and Detector

3.1 Large Hadron Collider

The Large Hadron Collider (LHC) [15] is the world's largest and most powerful particle accelerator ever built, located at CERN. It has 27 kilometre circumference, lies in a tunnel 100 metres below the France-Switzerland border. There are four large experiments currently running at the LHC and several more specialized experiments. The first two experiments in the LHC are the ATLAS experiment and the CMS experiment, which use a general-purpose detector to discover new physics. These two experiments use a different designed detector and do the research independently, competing with each other and also cross-checking the results from the other experiment at the same time. The next one is the ALICE experiment, designed specially for heavy-ion collisions. Its objective is to study quantum chromodynamics in detail, such as quark-gluon plasma state or the origin of confinement. The last of the 4 main experiments in LHC is the LHCb experiment. Its detector designed solely for the detection of B-mesons, to investigate the CP violation and explain why our universe is dominated by the matter, and not the anti-matter.

The LHC machine is proposed to reach the maximum capability at 14 TeV center-of-mass energy and 10^{34} cm^{-2}s^{-1} luminosity. The proton current in the LHC is not continuous, but rather divided into 2808 proton bunches per revolution. Each bunch contains 1.15×10^{11} protons, with 7 TeV energy per proton. The LHC is also capable of accelerating and colliding heavy ion, in this case Pb,
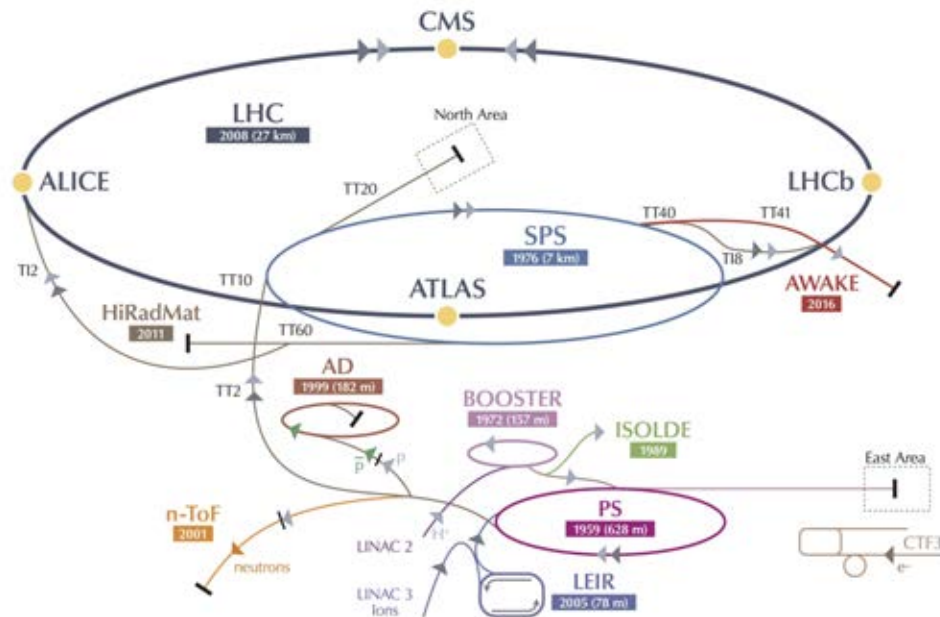
Figure 3.1: Map of CERN accelerator complex (not to scale) [16].

with the energy 2.76 TeV/nucleon and 10^{27} cm^{-2}s^{-2} luminosity. Protons for LHC are accelerated by CERN's accelerator complex as shown in Fig. 3.1, which will increase their energy step by step. The protons are acquired by removing electron from hydrogen atom then accelerated to 50 MeV through the LINAC2 accelerator. The protons are then injected to 4 rings of the Proton Synchrotron Booster (PS Booster) which will increase energy of each proton to 1.4 GeV, these protons will be sent to Proton Synchrotron (PS) to accelerate further more to 25 GeV. Lastly, the protons will be sent to Super Proton Synchrotron (SPS) where they are accelerated to 450 GeV before transferring to LHC which will increase their energy to the designed value.

The LHC machine successfully started the first beam on September 10, 2008, but it had to be halted again due to the electrical accident which later caused the helium leakage in the beampipe on September 19, 2008 [17]. After a year of repairing and testing, the LHC had begun its full research operation on March 30, 2010 with 7 TeV center-of-mass energy. From 2010 to 2011, the performance of LHC has been improved from 368 bunches per revolution with 150 ns bunch spacing to 1380 bunches with 50 ns bunch spacing. With the great performance

in 2010-2011, the LHC has been pushed furthermore by increasing the energy up to 8 TeV center-of-mass energy. The designed performance and the archived performance at the end of 2011 and 2012 are shown in Table 3.1 [18]. After 2 months of p-Pb run in early 2013, the LHC has entered the first long shut down phase for upgrading machine. The LHC is scheduled to start the operation again in early 2015 with 13 TeV center-of-mass energy.

Parameter	Design	End of 2011	End of 2012
Center of mass energy [TeV]	14	7	8
Bunch spacing [ns]	25	50	50
No. of bunches	2808	1380	1380
No. of protons per bunch [$\times 10^{11}$]	1.15	1.35	1.6
Peak luminosity [$\times 10^{33} \text{cm}^{-2}\text{s}^{-1}$]	10	2.44	7.7
Integrated luminosity [fb^{-1}]		5.6	23.3

Table 3.1: LHC beam parameters of p-p collisions at design performance compared to at the end of 2011 and 2012 [18].

3.2 Compact Muon Solenoid

The Compact Muon Solenoid detector (CMS) is one of the detectors at the LHC accelerator. It is a large scale general purpose detector, designed to explore a wide range of physics at the TeV scale. It is located in the underground cavern near Cessy in France. The CMS detector has a cylindrical shape with 21.6 metres long and 14.6 metres wide, weighs about 12,500 tonnes [20]. It is built like an onion, where each type of detector is placed in successive layer. Fig 3.2 shows the overall picture of the CMS detector, most of the detectors are packed inside a large super-conducting solenoid magnet which produces an enormous amount of magnetic field of 4 Tesla. The innermost layer of the CMS detector is a tracker which measures the momentum of charged particles, followed by electromagnetic calorimeter which absorbs and measures energy of electrons and photons and hadronic calorimeter which measures the hadronic particles. The last detector and the only detector
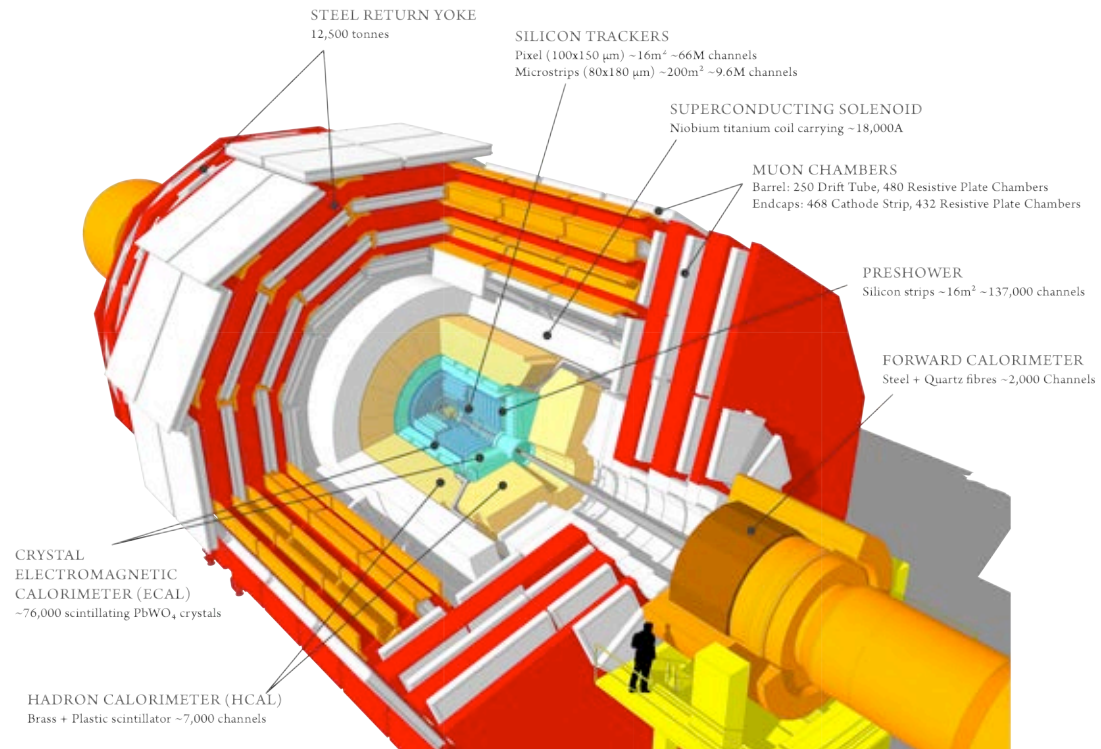
Figure 3.2: Sectional view of the CMS detector, shows each layer of subdetector from the inner most tracker to the muon chamber [19].

that is placed outside of the solenoid magnet is the muon system which is used to detect muons that can escape calorimeter. Since this muon system is still under the magnetic field of the superconducting solenoid, this enables us to measure the momentum of muon and combine the result with tracker, resulting in a better momentum resolution for muons.

The coordinate system in the CMS detector is defined as a Cartesian coordinate with right-handed system where the origin is located at the interaction point. The x-axis points into the center of the LHC ring while the y-axis points upward to the surface. The z-axis, as follow by right-handed system, points along the beam-line (counter-clockwise as view from above). The azimuthal angle ϕ is an angle in xy-plane measured from positive x-axis, and the polar angle θ is measured from positive z-axis. The pseudorapidity, η, is defined as $\eta = -\ln\tan(\theta/2)$. It is approximately the same as rapidity, y, in near speed of light limit. The pseu-

dorapidity is preferred to θ as a spatial coordinate because the production rates of particles in collider are roughly flat as a function of η, and the difference of pseudorapidity between two particles is also independent of Lorentz boost along the beam axis [21].

3.2.1 Magnet system

The magnet system plays the crucial role in measuring the momentum of charged particles. The CMS detector uses a large solenoid superconducting magnet to create 4 T magnetic field inside the detector. The benefit of using a strong magnetic field is that it gives a high resolution of charged particles' momentum in the tracker, and magnetic field outside the solenoid is still strong enough, allowing more layers of muon detector which help identifying muons and measuring their momenta. Furthermore, a good momentum resolution in the tracker also allows a better calibration for the electromagnetic calorimeter [22]. The solenoid magnet is 12.5 metres long, and 6.3 metres inner diameter. It uses high purity aluminium conductor with 4 layers winding (2,168 total number of turns), and has 19.5 kA operational current. The magnetic flux generated by superconducting solenoid will return via the saturated iron yoke. The barrel yoke is a 4-layer cylinder cover the outside of the magnet. The 2 endcap yokes are 3-layer disk placed at both ends of the solenoid coil.

The high magnetic field gives a high resolution of charged particles' momentum and also allows more layers of muon detector outside the magnet which help identify muons from the interactions.

3.2.2 Inner tracking system

The inner tracking system [23] is placed in the heart of the CMS detector, closest to the interaction point. It is used to track the position of charged particles as it flies out from the interaction point, and to reconstruct their path to determine the momenta of those particles. Since it is placed very close to the interaction point,
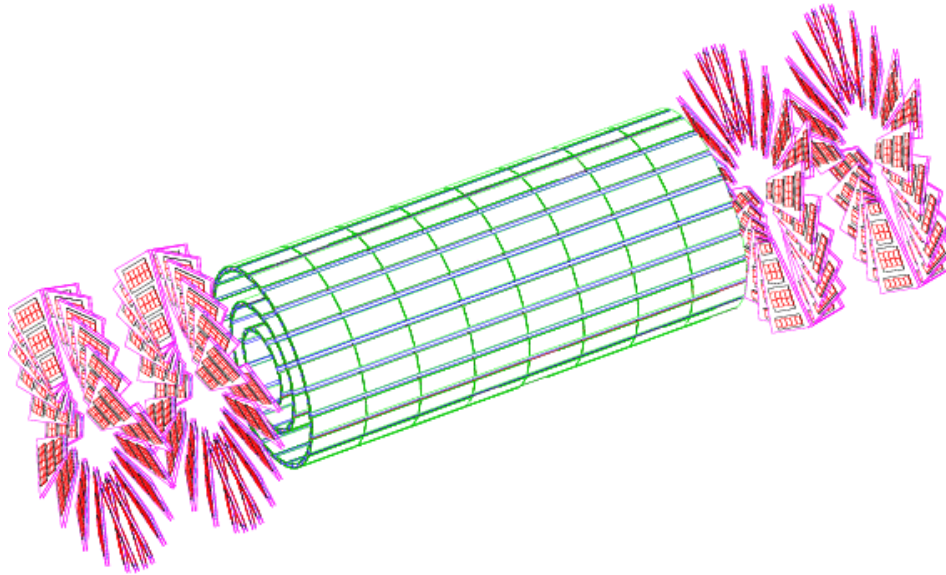
Figure 3.3: Layout of pixel detectors in the CMS tracker

it will be hit by a high flux of charged particles. To keep the low occupancy, we partitions the tracker into 3 regions. At radii below 10 cm, pixelated detector with $100{\times}150$ μm^2 size are used, resulting in the occupancy on the order of 10^{-4} per pixel per bunch crossing. The intermediate region (20 cm $< r <$ 55 cm) where particle flux is low enough, enables us to use the silicon microstrip tracker with the size of 10 cm$\times$80 μm with occupancy of 2-3% per strip per bunch crossing. In the outer most region of the inner tracker, particle flux has dropped sufficiently to allow a larger strip.

Pixel detector

The pixel detector is located at the innermost of the inner tracking system. It consists of 3 barrels and 2 endcap disks on each side, covering psudorapidity $-2.5 < \eta < 2.5$. The barrel part is 53 cm long and are placed at radii 4.4, 7.3, 10.2 cm. These barrels are made of 704 full modules and 96 half modules. The full modules are 65.9 mm long and 17.45 mm wide, and have 2 rows of 8 readout chips with $52{\times}80$ pixels of size $100{\times}150$ μm^2 each. The half modules are the same size but have only one row of readout chips. The 4 endcap disks cover
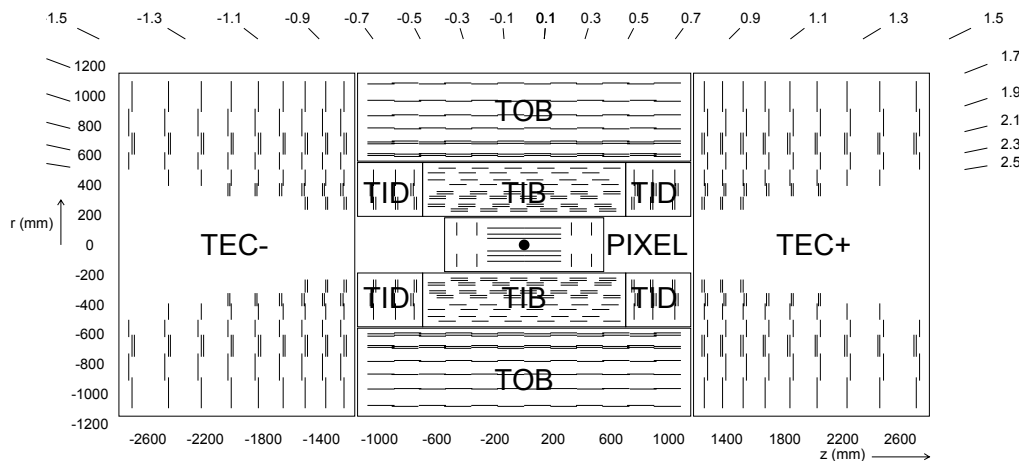
Figure 3.4: Schematic cross section in r-z plane of CMS tracker. Each line represents a detector module.

from radius 60 mm to 150 mm and are placed at $z = \pm 32.5, \pm 46.54$ cm. The sensor blades on the endcap disk are arranged like a turbine, where each blade is rotated by 20°. Each blade has 7 sensor arrays with 2 to 10 readout chips. In total, the pixel detector has approximately 66 million pixels covering the area of 1.06 m^2.

Silicon strip tracker

The layout of silicon strip tracker is shown in Fig 3.4. It is composed of a barrel region and two endcap regions. The barrel is divided into 2 parts, a tracker inner barrel (TIB) and a tracker outer barrel (TOB). TIB consists of 4 layers of concentric cylinder placed at radii of 255.0 mm, 339.0 mm, 418.5 mm, and 498.0 mm. The strip tracker in this region is 320 μm thick and 130 cm long. The first two layers have double-sided layers of 80 μm strip pitch, while the other two layers have a wider pitch of 120 μm with only a single sided layer. TOB has 6 layers of detector distributed in $600 - 1100$ mm radii range and cover up to $|z| < 110$ cm. The low radiation rate in this zone allows for the thicker (500 μm) and the wider pitch ($120 - 180$ μm) for silicon strip. The tracker endcaps (TEC) consist of 9 disks on each end, placed in between 120 cm $< |z| <$ 280 cm. Each disk extends

from $r = 229$ mm for the first three disks and 309 mm for the rest to outer radius of 1,135 mm. The first three disks have thickness of 320 μm and 500 μm for the rest. Pitch for the strip tracker in TEC varies from 96 μm to 183 μm. In addition, we have 3 other disks, called tracker inner disk (TID), to fill the void between TEC and TIB. These TIDs are 320 μm thick and have pitch varied from 97 μm to 143 μm. These silicon strip trackers also cover pseudorapidity in the range of $-2.5 < \eta < 2.5$.

3.2.3   Electromagnetic Calorimeter

Electromagnetic calorimeter (ECAL) [24] is the detector that is used to stop electrons and photons and measures total deposit energy from those particles. Lead tungstate (PbWO$_4$) has been chosen as a material for ECAL because of its short radiation range ($X_0 = 0.89$ cm) and small Molière radius (2.2 cm). This makes calorimeter very compact and has a fine granularity. Lead tungstate also has a very short scintillation decay time where 80% of light is released within 25 ns of bunch crossing time for LHC. One drawback of using lead tungstate as a scintillator is that it emits relatively low light yield (30 γ/MeV), this requires photodetector to have an intrinsic gain to detect the scintillation light. Silicon avalanche photodiodes (APDs) have been chosen as photodetectors in the barrel part ($|\eta| < 1.479$), and vacuum phototriodes (VPTs) for the endcaps ($1.479 < |\eta| < 3.0$). The lead tungstate crystals in barrel part have been manufactured in the shape of truncated square pyramid at $\eta = 0$. The cross-section dimension of the crystals is 0.0174$\times$0.0174 in η-ϕ, or 22$\times$22 mm^2 at the front face and 26$\times$26 mm^2 at the rear face. The crystal is 230 mm long, corresponding to 25.8 X_0. At a higher η, crystals' shape will be distorted along the radial line. In the endcaps, all crystals are made identical with the fixed cross section of 28.6$\times$28.6 mm^2 and 220 mm long. They are arranged in x-y grid instead of η-ϕ grid. A preshower (PS) device is placed in front of each endcap to identify neutral pions and improve the position determination of electrons and photons. It consists of lead radiators with $3X_0$ thick and 2 silicon strip sensors place at $2X_0$ and $3X_0$.
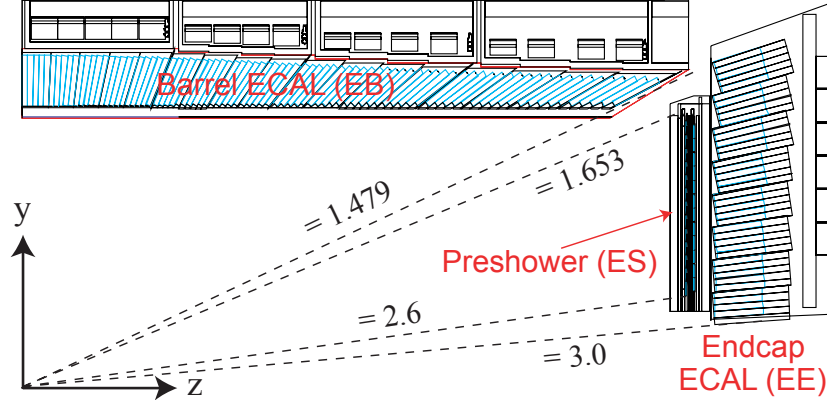
Figure 3.5: Cross section in r-z plane of electromagnetic calorimeter, showing the layout of the crystal modules.

3.2.4 Hadronic Calorimeter

Since the hadronic calorimeter (HCAL) [25] has to be confined in between the outer radius the elctromagnetic calorimeter ($r = 1.77$ m) and the inner radius of the solenoid ($r = 2.95$ m). The calorimeter choice has been narrowed down to the sampling type which can maximize the material in the limited space. Brass has been chosen as an absorber material due to its short interaction length and non-magnetic property. Like other parts of detectors, hadronic calorimeter also has two main parts that are hadron barrel and hadron endcaps. Furthermore, the hadron outer has been installed outside of the solenoid to capture particles that escape from the barrel part. To capture particles that travel with small angle along the beam line, an additional hadron forward has been installed at 11.2 m away from the interaction point with pseudorapidity covering up to $|\eta| < 5$.

Hadron Barrel

The Hadron barrel (HB) covers the pseudorapidity $|\eta| < 1.3$. There are 16 layers of absorber, 8 layers of 50.5-mm-thick brass plates and 6 layers of 56.5-mm-thick brass plates. The other 2 layers are steel plate with 40 mm thick covers the front and 75 mm thick covers the rear. The total interaction length in HB is 10.6 λ_I with an addition of 1.1 λ_I from the ECAL. The first scintillator uses 9 mm thick Bicron
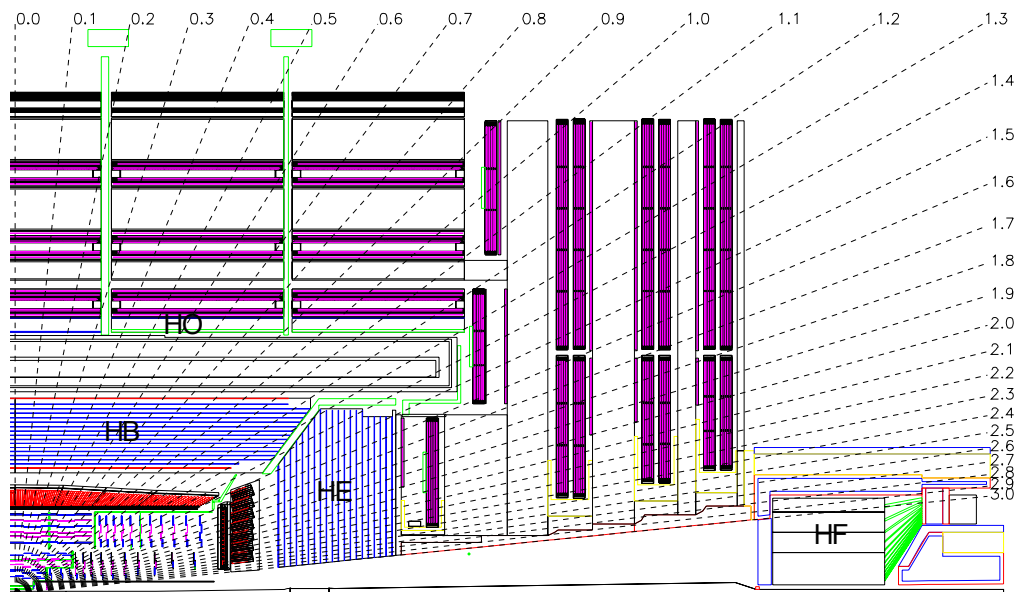
Figure 3.6: Longitudinal view of CMS detector showing the locations of the hadron barrel (HB), endcap (HE), outer (HO), and forward (HF) calorimeters. Dashed-lines show the psuedorapidity range of each part.

BC408 plastic, placed in front of the steel plate to capture showers generated from material between ECAL and HCAL. The rest of the scintillators use 3.7 mm thick Kuraray SCSN81 plastic placed between each absorber layers. The scintillators have been divided into 72 sectors in ϕ and has 32 longitudinal towers, resulting in the 0.087×0.087 size in (ϕ,η) for each readout cell.

Hadron Endcaps

The Hadron Endcaps (HE) cover the $1.3 < |\eta| < 3$ range. Brass plates used in this region are 79 mm thick assembled with 9 mm gaps for the insertion of scintillators. The total interaction length is about 10 λ_I (includes material from ECAL). The scintillators in the endcaps are segmented into $\Delta\eta \times \Delta\phi = 0.087 \times 0.087$ for $|\eta| < 1.6$ and $\Delta\eta \times \Delta\phi \approx 0.17 \times 0.17$ for $|\eta| \geq 1.6$.

Hadron Outer

The Hadron Outer (HO) is placed outside of the superconducting solenoid. It uses the solenoid as an additional absorber to detect any particles that can escape HB. The design of HO is constrained by the layout of the muon system. The return yoke is built into 5 rings labeled as number -2, -1, 0, 1, and 2. A HO scintillator is placed as the first layer in each of these 5 rings, except ring 0 in the middle which has 2 layers of scintillator separated by a 19.5 cm thick iron plate. This extends the total depth of the calorimeter system to 11.8 λ_I. The size and position of scintillator tiles are supposed to match those in the HB. Each tile is 10 mm thick and span 5° or 0.087 radian in ϕ, but the longitudinal division has to be confined with the five rings of yoke. This makes η-division in each ring varied from 8 divisions in ring 0, 6 divisions in ring ±1, and 5 divisions in ring ±2.

Hadron Forward

The Hadron Forward (HF) is placed at 11.2 m away from the interaction point. It is used to capture particles that are very close to the beamline ($3 < |\eta| < 5$). In this region, the calorimeter receives an unprecedented high particle flux, which makes the design of HF very challenging. For this reason, quartz fibres were chosen as the active material. The quartz fibres are composed of 600 μm-diameter fused-silica core covered by the polymer hard-cladding and the protective acrylate buffer. More than 1000 km of fibres are used in HF calorimeters. The HF consists of 165 cm ($\approx 10\lambda_I$) deep steel cylindrical absorber with 130.0 cm radius, and a hole of radius 12.5 cm for the beam pipe. The quartz fibres are put through the steel parallel to the beam pipe, forming a 5×5 cm^2 grid. Half of the fibres are put all along the full depth of steel absorber, while the other half are pulled back by 22 cm from the surface. These short and long fibres are used to distinguish the signal of electrons and photons from those of hadrons. Signal are generated when charged particles pass through the core of fibre and generate Cherenkov light (The light that emits from source which travels faster than speed of light in the medium).

Only a small fraction of the generated light which hit the core-clad surface with an angle larger than the critical angle will be collected and transported to the photomultiplier.

3.2.5 Muon System

Muon is the only detectable particle that can escape the calorimeters. The muon system [26] is placed in the outermost layer of the CMS detector, outside of the solenoid, to detect and identify the escaped muon. With an outstanding performance of the magnet, the return field is strong enough to provide an additional information about the momentum of the muon. The muon system consists of 3 types of detector. In the barrel part with low muon rate, low background, and low magnetic field, drift tube (DT) chambers are used. In the endcaps where there are higher in all muon rate, background, and magnetic field, cathode strip chambers (CSC) are chosen instead. In additional to these two detectors, the lower spatial resolution but fast response resistive plate chambers (RPC) are deployed in both barrel and endcaps to improve the time resolution for bunch crossing identification.

Barrel region

The barrel region covers $|\eta| < 1.2$ and consists of 4 concentric drift tube chamber cylinders. Each layer is segmented into 5 rings, follows the same layout of the return yoke. Each ring has 12 faces and each face has one drift tube chamber, except the outermost ring where the top and bottom faces have 2 chambers each. The drift tube chambers in the 3 inner rings have 3 superlayers, each consists of 4 layers of rectangular drift cell. The 2 outer superlayers have wires aligned parallel to the beamline, providing the track measurement in ϕ direction. Wires in the middle superlayer are orthogonal to the beamline measuring the z-position. The outer most rings have only 2 superlayers where the z-measuring superlayer is absent, thus providing only the ϕ coordinate. There are 6 layers of RPC in the barrel region following the same layout of the drift tube chambers. The two
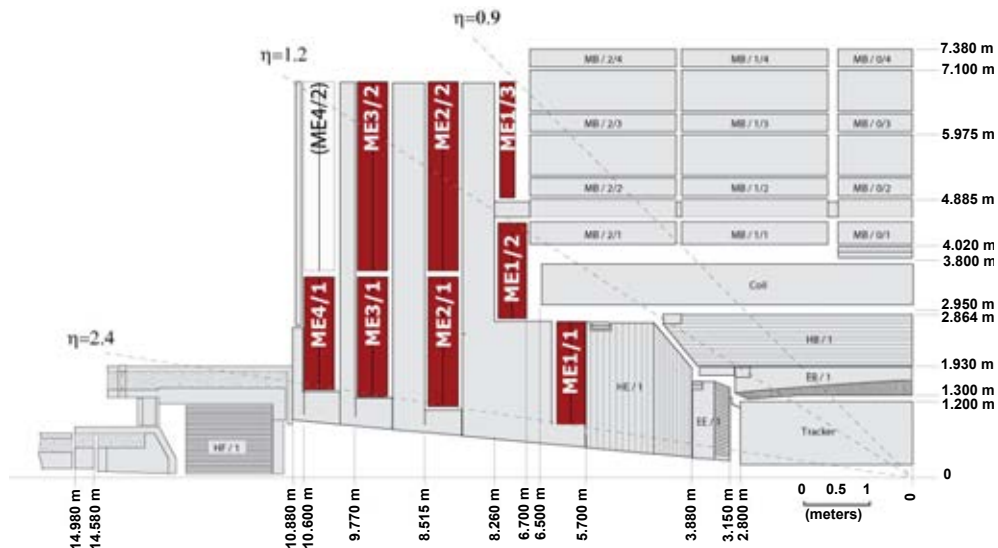
Figure 3.7: Quarter-view of the CMS detector showing the layout of CSC in the endcap of muon system.

inner drift tube chambers are sandwiched by two layers of RPC while the outer DT chambers will have only one RPC placed on the inner side.

Endcaps region

The CSCs in endcaps are produced in trapezoidal shape and cover either 10° or 20° in ϕ. The trapezoidal CSCs are then grouped into 9 groups of ME1/1, ME1/2, ME1/3, ME2/1, ME2/2, ME3/1, ME3/2, ME4/1, and ME4/2, forming a ring in each designed position as shown in Fig 3.7 (the ME4/2 chambers are not available in the early years of CMS operation). Each trapezoidal CSC comprises 7 cathode panels with 6 wire planes in between. The cathode strips are aligned along the radial line, providing the ϕ position, while the wires run azimuthally giving the radial coordinate. There are 3 layers of RPC in each endcap. They are placed behind ME1/2 and ME1/3, ME2/2, and ME3/2, covering up to only $|\eta| < 1.6$ in the initial stage of operation.

CHAPTER IV

Physics Object Reconstruction

4.1 Particle Flow Algorithm

The CMS detector has very strong magnetic field of 4 T, which gives a very good momentum resolution. Combined with a fine granularity of calorimeter, this enables the usage of particle flow (PF) [27] algorithm to reconstruct physics objects. The particle flow event reconstruction make use of various information from all subdetectors to reconstruct various types of detectable particles. The PF algorithm follows 4 steps. The track reconstruction and calorimeter clustering reconstruct hit signals in each detector into tracks and energy clusters. These tracks and energy clusters are then linked together to create a set of particle candidates. The last step is to classify these candidates into different physics objects such as electron, photon, or hadron.

4.1.1 Track Reconstruction

The track reconstruction algorithm can be explained in the following sequences [28]. The initial trajectory, called "seeds", are built using 2 or 3 hits in the pixel detector. These seeds are then extrapolated outward to the next tracker layer by finding the appropriate hit in that layer and extend the trajectory to the hit. These processes are repeated until the trajectory reaches the outer most tracker layer or meets a "stopping condition." These track-candidates are fitted again using the standard Kalman filter to remove the bias from the initial trajectory seed. The

track-candidates must pass a certain selection cuts to be considered as real tracks. To ensure the high tracking efficiency while retain low fake rate, an iterative tracking procedure has been adopted [29]. First the seed and track reconstruction are proceeded with very tight criteria, resulting in a moderate tracking efficiency with low fake rate. Hits corresponding to these tracks are removed and the track reconstruction process is executed again with looser criteria. With this, the track efficiency has been increased while the fake rate remains low from the removing of the hits in the previous step. This process is repeated iteratively to increase the efficiency of track reconstruction.

4.1.2 Calorimeter Clustering

The objective of this stage is to cluster the energy deposited in each calorimeter's cell into chunks of energy representing the energy deposit of each particle. First, the local maximum cells which have energy above a certain value are considered as "cluster seeds." The "topological clusters" are grown from cluster seeds by merging the cell nearby that share at least one side with the present cluster. These topological clusters are then risen as the "particle-flow clusters."

4.1.3 Link Algorithm

After we get the tracks and clusters, the next step is to link these elements into particle candidates called "blocks." Each block usually contains only one, two, or three elements. The smallness of block ensures that the algorithm's performance is independent of the complexity of events. The links between tracks and PS, ECAL, or HCAL are established by extrapolating the track to the matched elements, the link is valid only if the extrapolated track is within one cell away from the boundary of a cluster. The links between ECAL and HCAL or PS and ECAL are established in the same way. The links will be generated if the cluster of a more granular calorimeter (PS or ECAL) is within the cluster of a less granular calorimeter (ECAL or HCAL). Finally, the link between track in tracker and muon

track in muon system is established and fitted with an acceptance χ^2. When many tracks from tracker are linked to the same muon track, only the link with smallest χ^2 is chosen. These link blocks are then tagged as global muon.

4.1.4 Particle Identification

The final step is to identify the obtained blocks into different physics objects. First, each global muon will be marked as "particle-flow muon" if the combined momentum of muon is within 3 standard deviations from momentum calculated from tracker only. The tracks corresponding to particle-flow muon are removed from further consideration. The next step is the electron identification. Electrons are pre-identified by their characteristics of short track and energy loss by Bremsstrahlung in the tracker layers. The pre-identified electrons are then refitted with a Gaussian-Sum Filter [30] and passed through the final identification. Each identified electron will be tagged as a "particle-flow electron" and the corresponding track and ECAL cluster are removed. The remaining track will undergo a tighter criteria involving the uncertainty on momentum and calorimetry, the calibration of energy in ECAL and HCAL, the distance of extrapolated track to the linked ECAL or HCAL cluster etc. The compatibility between momentum and energy of the remaining track passing those criteria are considered. If momentum and energy of certain track are compatible, that track will be marked as a "particle-flow charged hadron." But if the calibrated energy is larger than acceptable uncertainty of momentum, those tracks will be marked as "particle-flow photon" or "particle-flow neutral hadron." Lastly, the remaining clusters of ECAL and HCAL with no corresponding track are also considered as "particle-flow photon" or "particle-flow neutral hadron" depending on the ECAL and HCAL components.

4.2 Jet Reconstruction

Jet is an object that represents the hadronized quark. It consists of many particles clustered together into one object. There are many clustering algorithms that are used in various experiments around the world. In CMS, the default algorithm is anti-k_t jet clustering [31] applied on particle-flow objects. In this algorithm, the distance variables for any two particles i and j are calculated:

$$d_{ij} = \min(k_{ti}^{-2}, k_{tj}^{-2}) \frac{\Delta_{ij}^2}{R^2}. \tag{4.1}$$

$$d_{iB} = k_{ti}^{-2}. \tag{4.2}$$

where d_{ij} is the distance between particle i and particle j, and d_{iB} is the distance between particle i and the beamline. $\Delta_{ij}^2 = (y_i - y_j)^2 + (\phi_i - \phi_j)^2$, where variables k_{ti}, y_i, and ϕ_i are the transverse momentum, rapidity, and azimuthal angle of particle i, respectively. The clustering process begins by finding the minimum value in collection of d_{ij} and d_{iB}. If d_{ij} is the minimum value, particle i and particle j are combined using a simple E-scheme recombination, which is just the sum of the two 4-momenta together. A new combined particle is added to the particle collection, while the two original particles will be removed. On the other hand, if d_{iB} is minimum, particle i will be tagged as "jet" and removed from the particle collection. The process is repeated until there is no particle left. To remove the fake jets, the jet identification (jet ID) criteria are applied to the jet collection. There are 3 levels of criteria, namely loose, medium, and tight. The list of variables and selection criteria for each level is shown in Table 4.1, where Neutral/Charged Hadron/EM Fraction is a fraction of energy deposited in Hadron/EM calorimeter by neutral/charged constituents.

B-Tagging

B-tagging plays a crucial role in many high energy analyses, including top quarks which decay dominantly into b quarks and W bosons. The tagging of b-jet is possible due to the unique characteristic of b-hadron (hadron that has b-quark as

PF Jet ID	Loose	Medium	Tight
Neutral Hadron Fraction	<0.99	<0.95	<0.90
Neutral EM Fraction	<0.99	<0.95	<0.90
Number of Constituents	>1	>1	>1
And for $\eta < 2.4$, $\eta > -2.4$ in addition apply			
Charged Hadron Fraction	>0	>0	>0
Charged Multiplicity	>0	>0	>0
Charged EM Fraction	<0.99	<0.99	<0.99

Table 4.1: The loose, medium and tight PF Jet ID criteria [32].

a constituent) that has long life time, which leads to a secondary vertex, and large multiplicity of charged particles in final state. Many b-tagging algorithms have been implemented already in CMS software. In this thesis, we will use a combined secondary vertex algorithm [33] to distinguish b-jets from the other jets. The b-discriminator, d, of this algorithm is defined as;

$$d = f_{BG}(c) \times \frac{\mathcal{L}^b}{\mathcal{L}^b + \mathcal{L}^c} + f_{BG}(q) \times \frac{\mathcal{L}^b}{\mathcal{L}^b + \mathcal{L}^q}. \tag{4.3}$$

where b and c stand for b-jets and c-jets, while q stands for u,d,s-quark jets and gluon jets. $f_{BG}(c)$ and $f_{BG}(q)$ are the probabilities that non-b jets have c or q contents ($f_{BG}(c) + f_{BG}(q) = 1$). $\mathcal{L}^{b,c,q}$'s are the Likelihood functions that give the likelihood that a certain jet is b, c, or q-jet, respectively. The Likelihood function is constructed from various variables, such as the type of secondary vertex, the impact parameter, the jet kinematics etc. The jets must have b-discriminator larger than a certain value to be considered as b-jets. The cut value is chosen by considering the requirements for tag efficiency versus the fake tag rate. The higher cut for b-discriminator gives a better rejection of non-b jets but also reduces the efficiency of b-tagging rate. By lowering the cut, we can get a better b-tag rate, but also allow more non-b jets to be tagged as b-jets.

CHAPTER V

Analysis

5.1 Monte Carlo Samples

The details of Monte Carlo samples used in this thesis are listed in Table 5.1. All samples are generated as 7 TeV center-of-mass energy proton-proton collisions from Summer11 productions except $t\bar{t}$ sample which comes from Fall11 productions. The signal sample is SUSY signal simulated at LM9 test point of mSUGRA model. The backgrounds can be differentiated into 3 general groups. The top backgrounds which include both $t\bar{t}$ and single top from all s-channel, t-channel, and tW-channel. The QCD multijet background with $\hat{p}_T$ range of $170 - 1800$ GeV, which have the corresponding integrated luminosity varied from hundreds pb^{-1} to hundreds fb^{-1}. Lastly, The electroweak backgrounds which consist of W boson decays into lepton and neutrino events, Z/γ^* to dilepton events, and diboson events. All samples are scaled to 183 pb^{-1} integrated luminosity.

5.2 Events Selection

High level trigger

The HT_MHT triggers are used in this thesis. HT in the trigger level is defined as the scalar sum of transverse momentum of all calo-jets with corrected $p_{\mathrm{T}} > 40$ GeV and $|\eta| < 3.0$, while MHT is the negative vector sum of all jets with corrected $p_{\mathrm{T}} > 30$ GeV and $|\eta| < 3.0$. All triggers are listed as follows:

Dataset	σ (pb)	Order	$\int \mathcal{L}\mathrm{d}t$ (fb^{-1})
QCD_Pt-XtoY_TuneZ2_7TeV_pythia6	varies		
TTJets_TuneZ2_7TeV-madgraph-tauola	158		25.3
T_TuneZ2_s-channel_7TeV-powheg-tauola	3.19	NNLO	81.5
Tbar_TuneZ2_s-channel_7TeV-powheg-tauola	1.44	NNLO	95.8
T_TuneZ2_t-channel_7TeV-powheg-tauola	41.92	NNLO	93.0
Tbar_TuneZ2_t-channel_7TeV-powheg-tauola	22.65	NNLO	85.9
T_TuneZ2_tW-channel-DR_7TeV-powheg-tauola	7.87	NNLO	103
Tbar_TuneZ2_tW-channel-DR_7TeV-powheg-tauola	7.87	NNLO	103
WJetsToLNu_250_HT_300_TuneZ2_7TeV-madgraph-tauola	34.8	LO	250
WJetsToLNu_300_HT_inf_TuneZ2_7TeV-madgraph-tauola	48.49	LO	111
DYJetsToLL_TuneZ2_M-50_7TeV-madgraph-tauola	3048	NNLO	11.9
WW_TuneZ2_7TeV_pythia6_tauola	27.83	LO	152
WZ_TuneZ2_7TeV_pythia6_tauola	10.47	LO	407
ZZ_TuneZ2_7TeV_pythia6_tauola	4.287	NLO	977
LM9_SUSY_sftsht_7TeV-pythia6	10.56	NLO	41.4

Table 5.1: The list of monte carlo samples with the corresponding cross-section and integrated luminosity.

- HLT_HT260_MHT60

- HLT_HT250_MHT60

- HLT_HT250_MHT70

- HLT_HT260_MHT80

The accepted events must pass at least one of the listed trigger above.

Selection Cuts

The initial cuts are taken from 1b-loose search region of CMS Analysis Note 2011/409 [34]. The selection cuts are chosen based on the hadronic decay of top quarks in supersymmetry signals. All events with at least one electron or muon with $p_{\mathrm{T}} \geq 10$ GeV and $|\eta| < 2.4$ are vetoed to remove the leptonic events. Events

are also required to have at least 3 good jets. Any PF jet will be considered as a good jet if it has $p_{\mathrm{T}} \geq 50$ GeV and $|\eta| < 2.4$, it is also required to pass the loose jet ID criteria. The four main cut variables that are of interest in this thesis are H_{T}, $E_{\mathrm{T}}^{\mathrm{miss}}$, $\Delta\phi_N^{\mathrm{min}}$, and number of b-jets.

The H_{T} variable is defined as a scalar sum of transverse momentum of all good jets ($H_{\mathrm{T}} = \sum_{\mathrm{good\,jets}} p_{\mathrm{T}}$). The $E_{\mathrm{T}}^{\mathrm{miss}}$ or missing transverse momentum is defined as the magnitude of the negative of vector sum of transverse momentum of all particles ($E_{\mathrm{T}}^{\mathrm{miss}} = |-\sum \vec{p}_{\mathrm{T}}|$). The presence of $E_{\mathrm{T}}^{\mathrm{miss}}$ variable indicates that there are particles that can escape from our detector, since momentum in the interaction must be conserved and there shouldn't be a transverse component from total momentum. This variable is very important in supersymmetry search because at the end of superpartner's decay chain, there should be the lightest supersymmetric particles (LSP) which are stable and don't interact with standard model's particle. These LSPs will escape the detector and give rise to $E_{\mathrm{T}}^{\mathrm{miss}}$.

b-quark is the key signal for the top quark physics, since top usually decays into b quark with 91 percent chance. The performance of b-tagging efficiency in CMS's data and MC are studied by the "b tag and Vertexing Physics Object Group" of CMS. For the combined secondary vertex algorithm, the group has recommended three working points to be used in the analysis; loose, medium, and tight working points. In this thesis, the combined secondary vertex at medium working point has been used to tag the b-jets. The b-discriminator cut value for this working point corresponds to the 99 percent rejection for non-b jets at $p_{\mathrm{T}} = 80\,\mathrm{GeV}$.

The $\Delta\phi_N^{\mathrm{min}}$ variable is used to discriminate the fake $E_{\mathrm{T}}^{\mathrm{miss}}$ from the real one. The fake $E_{\mathrm{T}}^{\mathrm{miss}}$ in QCD events is usually rooted from a large mismeasurement of a single jet's momentum. For this reason, the angle in transverse plane $\Delta\phi_j$ between jet j and $E_{\mathrm{T}}^{\mathrm{miss}}$ should be a very useful variable to discriminate events with real $E_{\mathrm{T}}^{\mathrm{miss}}$ from the fake $E_{\mathrm{T}}^{\mathrm{miss}}$ in QCD events. But unfortunately, the angle $\Delta\phi_j$ is highly correlated to $E_{\mathrm{T}}^{\mathrm{miss}}$. To reduce this effect, the normalized azimuthal angle

for jet j has been defined as:

$$\Delta\phi_{Nj} = \Delta\phi_j / \arctan\left(\Delta_{Tj}/E_\mathrm{T}^{\mathrm{miss}}\right), \tag{5.1}$$

and Δ_{Tj} is:

$$\Delta_{Tj} = 0.1 \frac{\sqrt{\sum_{i \neq j} \left[p_x^j p_y^i - p_y^j p_x^i\right]^2}}{p_\mathrm{T}^j}, \tag{5.2}$$

where the summation runs over all jets with the same criteria as good jets above, except the transverse momentum cut that has been loosen to 30 GeV. The $\Delta\phi_{Nj}$ variable is calculated for the first three leading good jets. The minimum value from these three jets is labelled as $\Delta\phi_N^{\mathrm{min}}$ and is used as the discriminator.

The initial cuts for these four variables are listed below:

- $H_\mathrm{T} > 400\,\mathrm{GeV}$

- $E_\mathrm{T}^{\mathrm{miss}} > 250\,\mathrm{GeV}$

- $\Delta\phi_N^{\mathrm{min}} > 4$

- number of b-jets ≥ 1

5.3 Characteristic and performance of the selection cuts

Fig 5.1 shows the distributions, plotted in log-scale, of H_T, $E_\mathrm{T}^{\mathrm{miss}}$, number of b-jets, and $\Delta\phi_N^{\mathrm{min}}$ before applying any cut on these variables. The distribution of H_T from backgrounds shows a sharp rising at low H_T until they reach the peak at H_T around 200 - 300 GeV then slowly decrease as H_T increases, except for QCD background which has peak at around 450 GeV, far higher than the other backgrounds. The distribution of H_T from LM9 signal is, however, relatively flat compared to the backgrounds. It has a peak at around 600 GeV. The characteristic of $E_\mathrm{T}^{\mathrm{miss}}$ is quite the same as that of H_T. The backgrounds have peaks at very
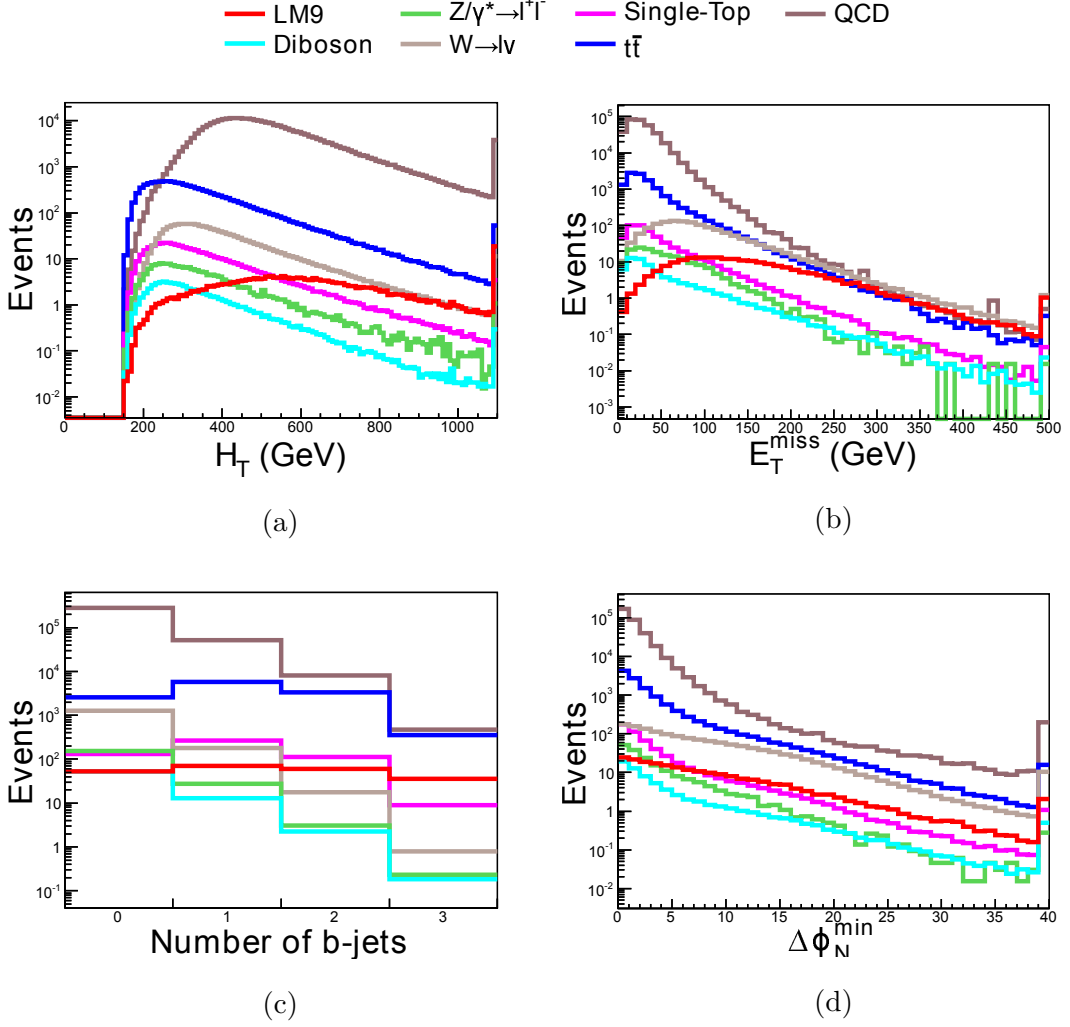
Figure 5.1: Distributions of (a) H_{T} (b) $E_{\mathrm{T}}^{\mathrm{miss}}$ (c) Number of b-jets (d) $\Delta\phi_N^{\mathrm{min}}$ before applying the selection cuts on these variable.

low $E_{\mathrm{T}}^{\mathrm{miss}}$ and decrease rapidly as $E_{\mathrm{T}}^{\mathrm{miss}}$ increases. This time, $W \to l\nu$ background and LM9 signal show a different shape from the other backgrounds. The peaks are located at higher $E_{\mathrm{T}}^{\mathrm{miss}}$ (60 GeV for $W \to l\nu$ and 100 GeV for LM9) and the distributions decrease more slowly than the backgrounds. As for the number of b-jets, the distributions of backgrounds still show an obvious difference to the signal. The number of events in all backgrounds decrease as the number of b-jets increases, even with the top background in which the distribution seems flat in the first three bins, but it still drops significantly in the forth bin. On the other hand, the LM9 signal shows a flat distribution in all range. The $\Delta\phi_N^{\mathrm{min}}$'s distributions

for signal and backgrounds look the same at first sight, all of them decrease as $\Delta\phi_N^{\min}$ increases. But if we look closely at the low $\Delta\phi_N^{\min}$ regions, the distributions from LM9 signal and $W \to l\nu$ background are a bit less steep than the other backgrounds.

To determine the performance of each cut variable, the ratio plots have been investigated. The distribution histogram of each variable before and after applying the cut are plotted with the same binning, the ratio of number of events before and after the cut in each bin ($N_{\text{after}}/N_{\text{before}}$) is calculated and put in the same bin of a new histogram. The ratio plots of each variable with each single cut are shown in Fig 5.2. The H_{T} variable shows, as seen from the number of b-jets plot, a good capability of discriminating against backgrounds other than QCD. It can suppress backgrounds down to only 30-40%, while retains the LM9 signal and QCD at around 80%. This cut is not very effective at $E_{\text{T}}^{\text{miss}} > 350$ GeV as the ratio rises to one. But it gives a better efficiency at higher $\Delta\phi_N^{\min}$ as it reduces background to only 20%.

The efficiency of $E_{\text{T}}^{\text{miss}}$ cut can be determined from, again, the number of b-jets plot in Fig 5.2 (e). The $E_{\text{T}}^{\text{miss}}$ cut can give a very high rejection rate which reduces all backgrounds to less than 3%, but also cut off a lot of signal at the same time leaving only 10% of LM9 events remaining. But the distributions of the other variables show that the effectiveness of this cut is lower as H_{T} and $\Delta\phi_N^{\min}$ are higher, especially for the high H_{T} region where the fluctuation is very high and the signal and backgrounds get mixed up.

Fig 5.2 (g)-(i) show the ratio plots applying only the number of b-jets cut. All of them show agreements on the effectiveness of number of b-jets cut. Almost all backgrounds are reduced to less than 30% at all range of all variables, leaving only top backgrounds which pass the cut at the same rate as LM9 signal at 80%. This is to be expected because b-jets are the signature of top events since almost all of them decay into b-quarks and W bosons.

The ratio plots of the last cut, $\Delta\phi_N^{\min}$, are shown in Fig 5.2 (j)-(l). The efficiency of the cut can be seen from number of b-jets plot. Most of the back-
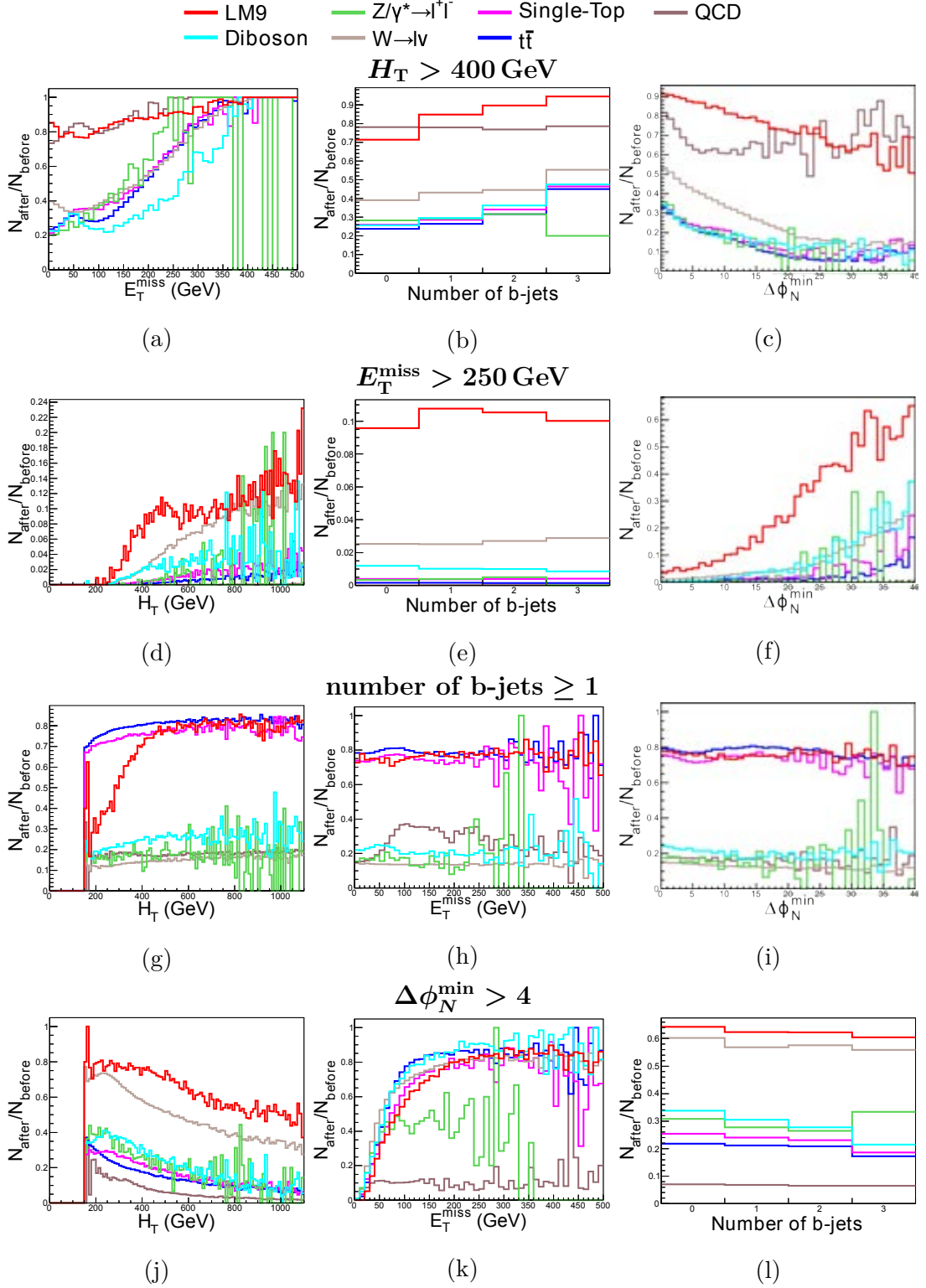
Figure 5.2: Ratio plot with only a single cut of (a)-(c) H_T, (d)-(f) E_T^{miss}, (g)-(i) number of b-jets, and (j)-(l) $\Delta\phi_N^{\mathrm{min}}$.

grounds are reduced drastically to only 20-35%, especially for QCD background which is suppressed to less than 10%. The only remaining events are LM9 signal and $W \rightarrow l\nu$ background which pass the cut at around 60% rate. Even though H_T and number of b-jets plots look clean and separate backgrounds from signal clearly, the $E_\mathrm{T}^\mathrm{miss}$ shows no difference at all between signal and background except QCD background which remains at 10% rate in all range. This can be explained by the fact that $\Delta\phi_N^\mathrm{min}$ is constructed especially to remove the fake $E_\mathrm{T}^\mathrm{miss}$ from the mismeasurement of jets' momenta in QCD events, resulting in the huge removal of QCD events, leaving only the events with the real $E_\mathrm{T}^\mathrm{miss}$.

Fig 5.3 shows the ratio plot of each variable after applying full selection cuts. All backgrounds are reduced drastically in H_T, number of b-jets, and $\Delta\phi_N^\mathrm{min}$, while the signal still remains with a significantly high ratio. In case of $E_\mathrm{T}^\mathrm{miss}$, the difference between signal and background is a bit clearer. Most of the backgrounds are reduced, especially for QCD which almost vanishes. The only background with high ratio left is the top backgrounds which has almost the same passing rate as LM9 signal.

5.4   Optimization

The goodness of our cuts is determined by calculating the the quality factor $Q = 2\left(\sqrt{N_S + N_B} - \sqrt{N_B}\right)$, where N_S and N_B is number of signal and background events [35]. This Q factor tell us how good the selection is, the higher value the better it is. The Q factor has better statistical properties than the usual "significance" $S_1 = \frac{N_S}{\sqrt{N_B}}$ or $S_2 = \frac{N_S}{\sqrt{N_S + N_B}}$. For $N_b \gg N_s$, the Q factor and the significance coincide ($Q \approx S_1 \approx S_2$). To optimize our cuts, one cut is varied at a time while keeping the other cut variables at fixed value, the Q factor is calculated for every varied cuts and plots into a histogram. By doing this, we can determine a certain cut value for each variable which gives the maximum Q factor. Fig 5.4 (a)-(d) show the plots of Q factor when varying each cut variable from our selection. The maximum in number of b-jets plot is located at 1 b-jet, the same as
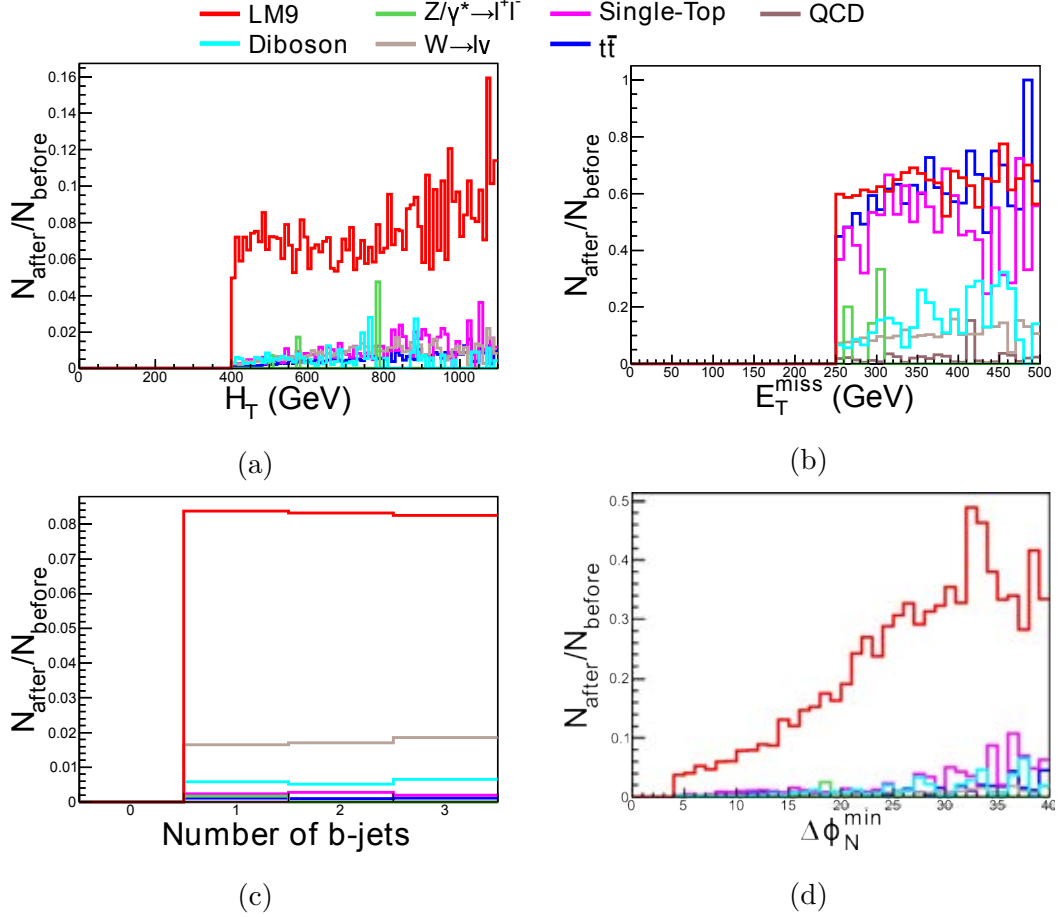
Figure 5.3: Ratio plots of (a) H_{T} (b) $E_{\mathrm{T}}^{\mathrm{miss}}$ (c) Number of b-jets (d) $\Delta\phi_N^{\mathrm{min}}$ with the full selection cuts.

our selection cut. The H_{T} and $\Delta\phi_N^{\mathrm{min}}$ plots show a slight difference between our cut points and the maxima of Q factor. The most difference between the cut and maximum comes from the $E_{\mathrm{T}}^{\mathrm{miss}}$ which reaches its maximum at $E_{\mathrm{T}}^{\mathrm{miss}} = 150$ GeV, far lower than the point where we put the cut. After the $E_{\mathrm{T}}^{\mathrm{miss}}$ cut is changed to $E_{\mathrm{T}}^{\mathrm{miss}} > 150$ GeV, the Q factor has been plotted again as shown in Fig 5.4 (e)-(h). The maximum in number of b-jets remains the same while $\Delta\phi_N^{\mathrm{min}}$'s has moved to $\Delta\phi_N^{\mathrm{min}} = 4$, the same point as our cut. The maximum point for H_{T} has increased to 440 GeV. After we repeatedly modify the cuts for H_{T} and $E_{\mathrm{T}}^{\mathrm{miss}}$ several more times, the optimized cut has been reached at $H_{\mathrm{T}} > 480\,\mathrm{GeV}$, $E_{\mathrm{T}}^{\mathrm{miss}} > 120\,\mathrm{GeV}$, number of b-jets ≥ 1, and $\Delta\phi_N^{\mathrm{min}} > 4$ as shown in Fig 5.6. By using these cuts, we can get the Q factor of 4.81 which is a lot better than $Q = 0.368$ before applying

any cuts and $Q = 2.97$ after applying the initial cuts.

The comparison between ratio plots of initial cuts and optimized cuts are shown in Fig 5.7. The overall ratios from every variable increase a lot after the optimization. The signal ratio in H_{T} plot has increased from around 10% to 30-40%, while the background ratio increases slightly to around 5%. The shape of ratio plot of $E_{\mathrm{T}}^{\mathrm{miss}}$ doesn't change much for both signal and background, but the range has been extended from 250 GeV down to 120 GeV which allows more LM9 signal to be included. The background rate in the extended range is also lower than background in $E_{\mathrm{T}}^{\mathrm{miss}} > 250$ GeV region. The signal ratio in number of b-jets' plot has also increased from less than 10% up to 30-35%. $W \to l\nu$ is the only background that has increased with a noticeable amount after the optimization, but the rate is still low compared to the signal. The ratio plot of $\Delta\phi_N^{\mathrm{min}}$ shows a good improvement of signal rate in low $\Delta\phi_N^{\mathrm{min}}$ region, while the signal rate in high $\Delta\phi_N^{\mathrm{min}}$ region is reduced a little bit. Fig 5.8 shows the distribution of H_{T}, $E_{\mathrm{T}}^{\mathrm{miss}}$, number of b-jets, and $\Delta\phi_N^{\mathrm{min}}$ after applying the optimized cuts. Most of the backgrounds are suppressed almost completely leaving only QCD, $t\bar{t}$, and $W \to l\nu$ to contribute to the shape of the distributions. The LM9 signal stands out clearly with 20% of total events in the distributions. The LM9 would be undoubtedly found in the real experiment if it really exists.

- $H_T > 400\,\text{GeV}$ • $E_T^{\text{miss}} > 250\,\text{GeV}$ • number of b-jets ≥ 1 • $\Delta\phi_N^{\text{min}} > 4$
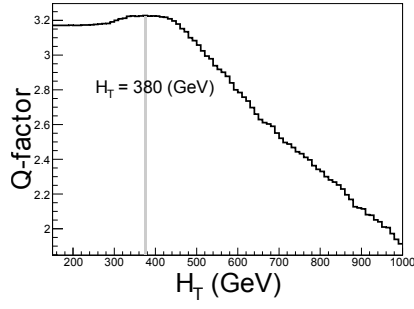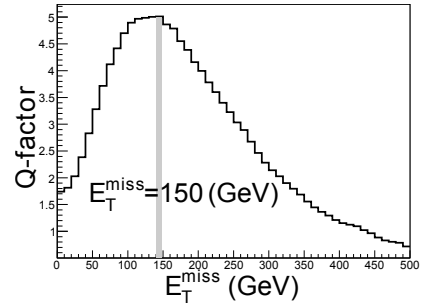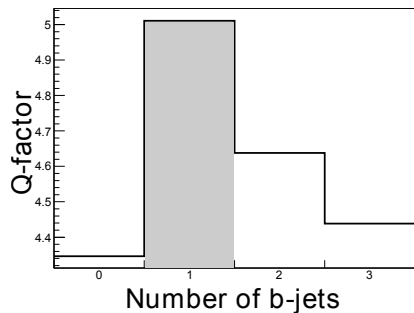

(a)
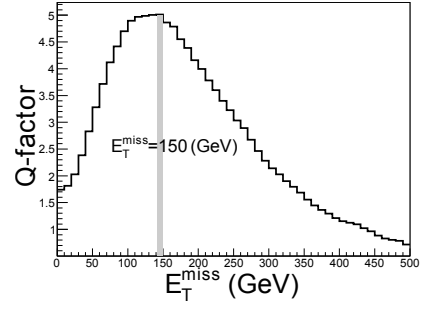
(b)
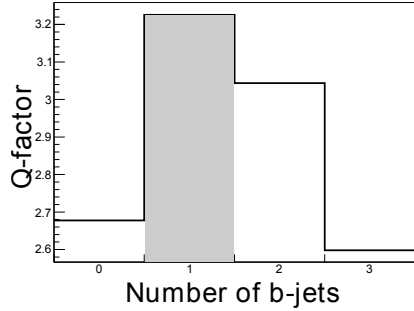
(c)
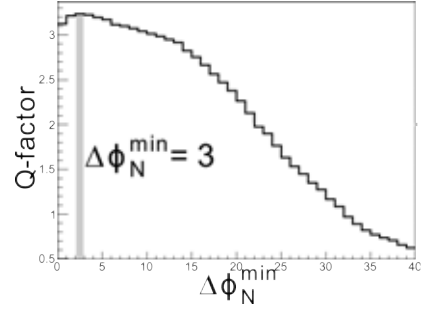
(d)

- $H_T > 400\,\text{GeV}$ • $E_T^{\text{miss}} > 150\,\text{GeV}$ • number of b-jets ≥ 1 • $\Delta\phi_N^{\text{min}} > 4$
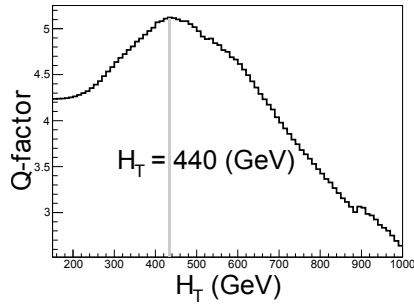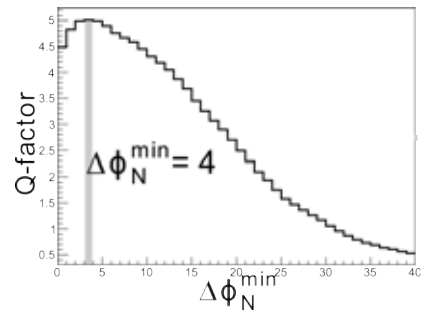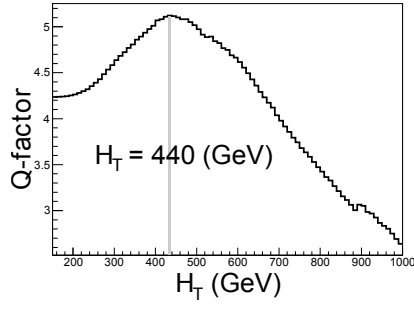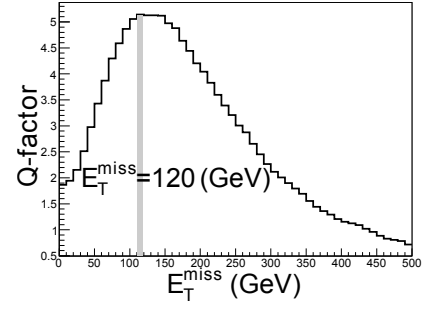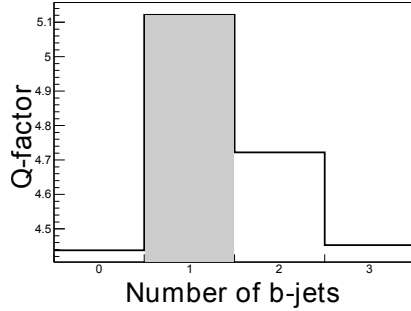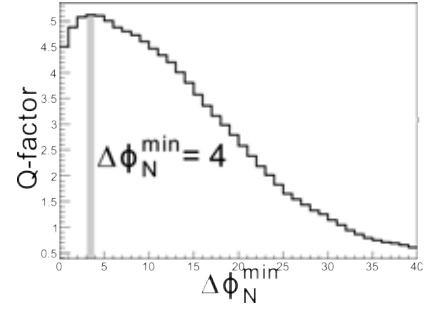

(e)

(f)

(g)

(h)

Figure 5.4: Quality factor of each varying cut of (a),(e) H_T (b),(f) E_T^{miss} (c),(g) number of b-jets (d),(h) $\Delta\phi_N^{\text{min}}$. The main cuts are listed above the plot. The gray strips indicate the maximum bin in each plot.

- $H_T > 440\,\text{GeV}$ • $E_T^{\text{miss}} > 150\,\text{GeV}$ • number of b-jets ≥ 1 • $\Delta\phi_N^{\text{min}} > 4$
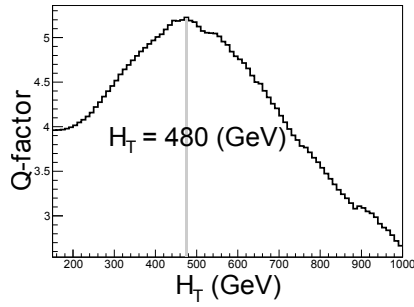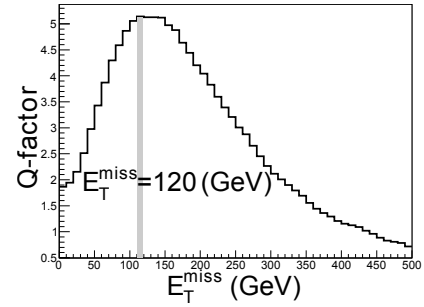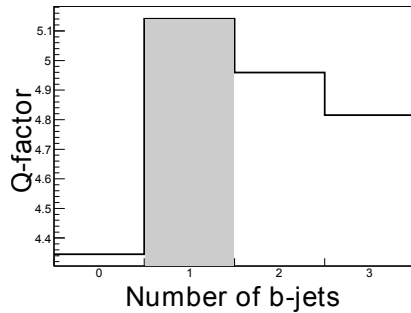

(a)

(b)

(c)

(d)

- $H_T > 440\,\text{GeV}$ • $E_T^{\text{miss}} > 120\,\text{GeV}$ • number of b-jets ≥ 1 • $\Delta\phi_N^{\text{min}} > 4$
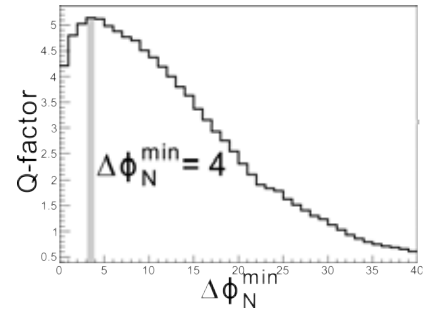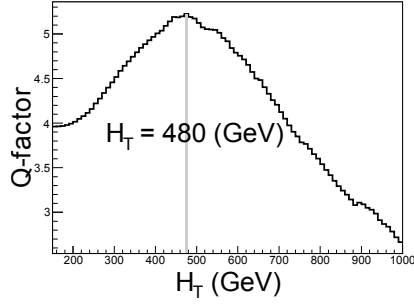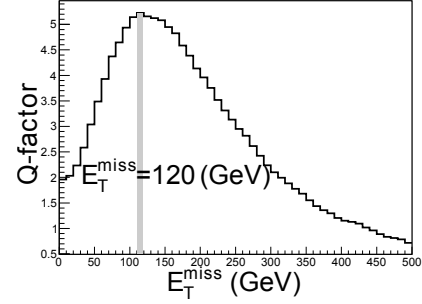

(e)

(f)

(g)

(h)

Figure 5.5: Quality factor of each varying cut of (a),(e) H_T (b),(f) E_T^{miss} (c),(g) number of b-jets (d),(h) $\Delta\phi_N^{\text{min}}$. The main cuts are listed above the plot. The gray strips indicate the maximum bin in each plot.

- $H_T > 480\,\mathrm{GeV}$ • $E_T^{\mathrm{miss}} > 120\,\mathrm{GeV}$ • number of b-jets ≥ 1 • $\Delta\phi_N^{\min} > 4$

(a)

(b)

(c)

(d)

Figure 5.6: Quality factor of each varying cut of (a) H_T (b) E_T^{miss} (c) number of b-jets (d) $\Delta\phi_N^{\min}$. The main cuts are listed above the plot. The gray strips indicate the maximum bin in each plot.
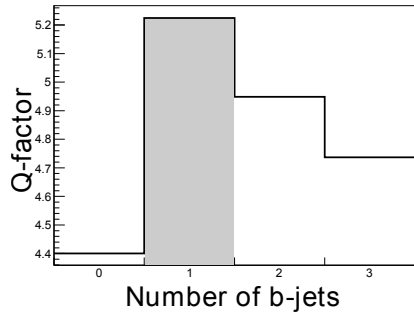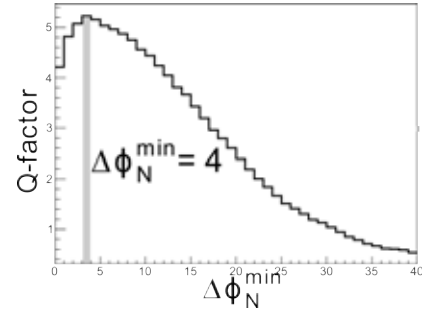
Figure 5.7: The comparison of ratio plots of (a),(b) H_{T} (c),(d) $E_{\mathrm{T}}^{\mathrm{miss}}$ (e),(f) number of b-jets (g),(h) $\Delta\phi_N^{\min}$ between the initial cuts and optimized cuts.
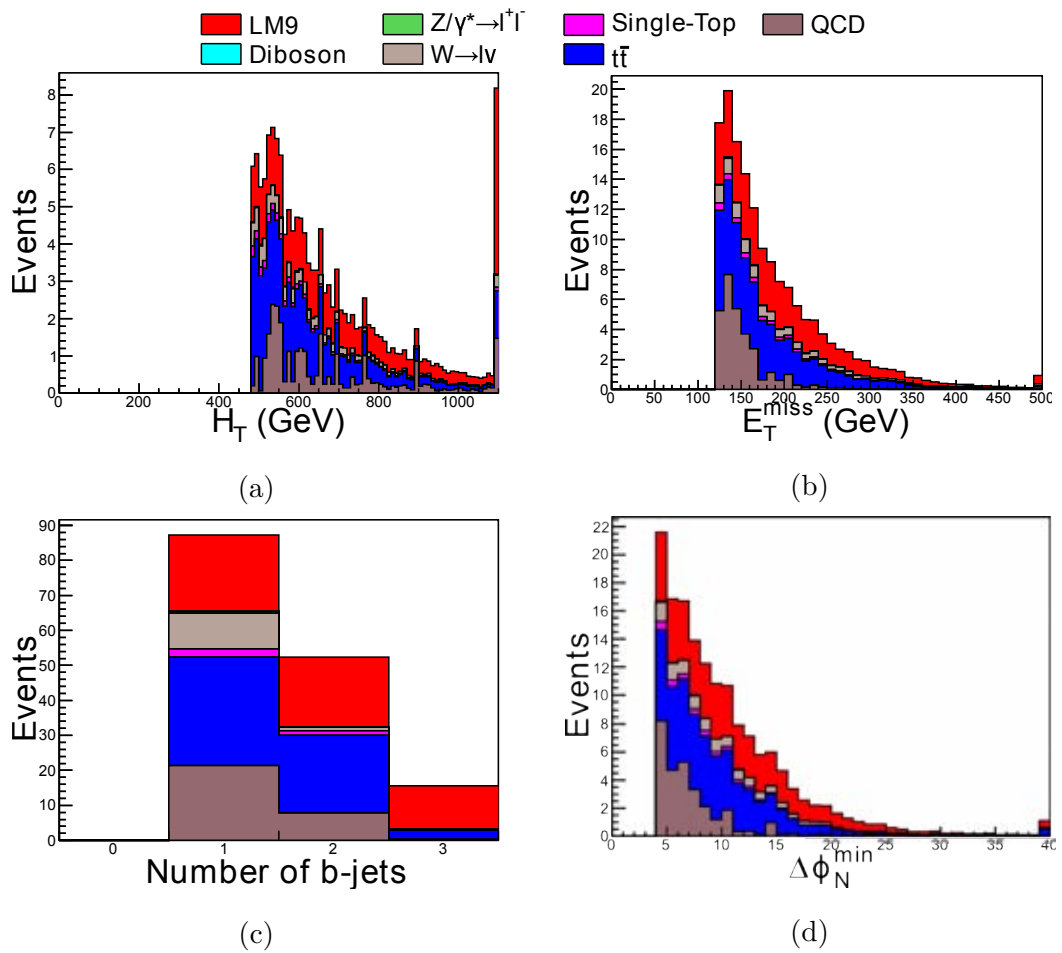
Figure 5.8: Distributions of (a) H_{T} (b) $E_{\mathrm{T}}^{\mathrm{miss}}$ (c) Number of b-jets (d) $\Delta\phi_N^{\mathrm{min}}$ after applying the optimized selection cuts.

CHAPTER VI

Conclusions

We have presented a search for supersymmetry events in hadronic channel at LM9 test point. The analysis was done using the Monte Carlo simulation normalized to an integrated luminosity of 183 pb^{-1}. The characteristics of four variables have been investigated. Each cut variable is proved to be useful against different types of background. When all the cuts are combined together, all backgrounds have been suppressed sufficiently while retain a reasonable amount of SUSY signal. After the optimization of quality factor, the efficiency has been improved as it allows more signal to pass the cuts while keeping high rejection rate for backgrounds. Quality factor has increased from 2.97 in the initial cuts to 4.81 after the optimization. After applying the cuts, the LM9 signal has stood out clearly compared to backgrounds.

References

[1] J. Beringer et al. (Particle Data Group), "Review of Particle Physics," Phys. Rev. D **86**, 010001 (2012)

[2] A. Purcell, "Go on a particle quest at the first CERN webfest." CERN Bulletin **35** (2012) `http://cds.cern.ch/journal/CERNBulletin/2012/36/News%20Articles/1473657`

[3] N. Agafonova et al. (OPERA Collaboration), "Observation of a first ν_τ candidate in the OPERA experiment in the CNGS beam," Phys. Rev. Lett. **B691**, 138 (2012) [arXiv:1006.1623 [hep-ex]]

[4] F. P. An et al. (Daya Bay Coll.), "Observation of electron-antineutrino disappearanceat Daya Bay," Phys. Rev. Lett. **108**, 171803 (2012) [arXiv:1203.1669 [hep-ex]]

[5] A. X. El-Khadra and M. Luke, "The Mass of the b quark," Ann. Rev. Nucl. Part. Sci. **52**, 201-251 (2002) [arXiv:hep-ph/0208114]

[6] V. D. Barger and R. J. N. Phillips, "Collider Physics (Frontiers in Physics)," Updated ed., Addison-Wesley Publishing Company (1997)

[7] W. Bernreuther, "Top quark physics at the LHC," J. Phys. G**35**, 083001 (2008) [arXiv:0805.1333 [hep-ph]]

[8] D. J. Griffiths, "Introduction to Elementary Particles," John Wiley & Sons (1987)

[9] ATLAS Collaboration, "Observation of an Excess of Events in the Search for the Standard Model Higgs boson with the ATLAS detector at the LHC," ATLAS-CONF-2012-093

[10] S. Chatrchyan et al.(CMS Collaboration), "Observation of a new boson at a mass of 125 GeV with the CMS experiment at the LHC," Phys. Lett. B **716**, 30 (2012) [arXiv:1207.7235 [hep-ex]]

[11] G. Aad et al.(ATLAS Collaboration), "Observation of a new particle in the search for the Standard Model Higgs boson with the ATLAS detector at the LHC," Phys. Lett. B **716**, 1 (2012) [arXiv:1207.7214 [hep-ex]]

[12] S. Dittmaier et al. (LHC Higgs Cross Section Working Group), "Handbook of LHC Higgs Cross Sections: 2. Differential Distributions," CERN-2012-002 [arXiv:1201.3084 [hep-ph]]

[13] S. P. Martin, "A supersymmetry primer," in G.L.Kane, Perspectives on Supersymmetry, pp. 1-98, World Scientific (1997) [arXiv:hep-ph/9709356]

[14] G. L. Bayatian et al. (CMS Collaboration), "CMS Physics: Technical Design Report Volume 2: Physics Performance," J. Phys. G **34**, 995 (2007) `https://cds.cern.ch/record/942733/`

[15] L. Evans and P. Bryant, "LHC machine," JINST **3**, S08001 (2008)

[16] J. Haffner, "The CERN accelerator complex," (2013) `https://cds.cern.ch/record/1621894`

[17] S. Myers, "THE LARGE HADRON COLLIDER 2008-2013," Int. J. Mod. Phys. A **28**, 1330035 (2013)

[18] R. Alemany-Fernandez et al., "Operation and Configuration of the LHC in Run 1," CERN-ACC-NOTE-2013-0041

[19] T. Sakuma, "3D SketchUp images of the CMS detector (120918)," CMS-doc-11514-v1

[20] S. Chatrchyan et al. (CMS Collaboration), "The CMS experiment at the CERN LHC," JINST **3**, S08004 (2008)

[21] G. L. Bayatian et al. (CMS Collaboration), "CMS Physics: Technical Design Report Volume 1: Detector Performance and Software," CERN (2006) `https://cds.cern.ch/record/922757`

[22] CMS Collaboration, "The CMS magnet project: Technical Design Report," CERN (1997) `https://cds.cern.ch/record/331056`

[23] V. Karimäki et al. (CMS Collaboration), "The CMS tracker system project: Technical Design Report," CERN (1997) `https://cds.cern.ch/record/368412`

[24] CMS Collaboration, "The CMS electromagnetic calorimeter project: Technical Design Report," CERN (1997) `https://cds.cern.ch/record/349375`

[25] CMS Collaboration, "The CMS hadron calorimeter project: Technical Design Report," CERN (1997) `https://cds.cern.ch/record/357153`

[26] CMS Collaboration, "The CMS muon project: Technical Design Report," CERN (1997) `https://cds.cern.ch/record/343814`

[27] CMS Collaboration, "Particle-Flow Event Reconstruction in CMS and Performance for Jets, Taus, and MET," CMS-PAS-PFT-09-001

[28] CMS Collaboration, "Track Reconstruction in the CMS tracker (in preparation)," CMS-PAS-TRK-09-001

[29] M. Pioppi, "Iterative Tracking," CMS Internal Note 2007/065

[30] CMS Collaboration, "Reconstruction of Electrons With the Gaussian-Sum Filter in the CMS tracker at LHC," CMS Note RN 2003-001

[31] M. Cacciari, G. P. Salam, G. Soyez, "The anti-k_t jet clustering algorithm," JHEP **04**, 063 (2008) [arXiv:0802.1189 [hep-ph]]

[32] A. Harel and P. Schieferdecker, "Jet Identification," (2012). `https://twiki.cern.ch/twiki/bin/viewauth/CMS/JetID`

[33] C. Weiser, "A Combined Secondary Vertex Based B-Tagging Algorithm in CMS," CMS Note 2006/014 (2006)

[34] J. W. Gary et al., "Search for New Physics in Events with b-jets and Missing Transverse Energy with the full 2011 Data Sample," CMS Analysis Note 2011/409 (2012)

[35] S. I. Bityukov and N. V. Krasnikov, "Towards the Observation of Signal over Background in Future Experiments," Preprint INR 0945a/98 (1998) [arXiv:physics/9808016 [physics.data-an]]

APPENDIX

APPENDIX A

Quality Factor

In high energy physics, the commonly used significant variables for determining the possibility to discover new physics are $S_1 = \frac{N_S}{\sqrt{N_B}}$ and $S_2 = \frac{N_S}{\sqrt{N_B + N_S}}$, where N_S and N_B are number of signal and background events. The difference between S_1 and S_2 is based on the concept of "real" and "future" experiments. It is usually claimed that new physics will be discovered if we have an excess of events larger than 5σ. If the probability of getting n events can be explained by Poisson distribution, then the standard deviation σ will be $\sqrt{<N>}$ where $<N>$ is the predicted number of events. In the "real" experiment, we know the exact number of all events we got (N_{ev}), then the number of possible signal can be determined from $N_S = N_{ev} - <N_B>$. In this case, the standard deviation comes from number of background events only and the significance becomes $S_1 = \frac{N_S}{\sigma} = \frac{N_S}{\sqrt{N_B}} > 5$. But in case of "future" experiment, we have to model both background and signal, the standard deviation becomes $\sqrt{<N_B> + <N_S>}$ and we have to use S_2 instead. For $N_B \gg N_S$, the significances S_1 and S_2 are approximately the same.

The new significance, Q factor, are developed based on the probability that the "standard physics" can imitate the signal of "new physics". The probability distribution for both model can be explained by Poisson distribution with the expected number of events $<N_B>$ for standard physics and $<N_B> + <N_S>$ for the new physics. In case of $<N> \gg 1$, the Poisson distribution can be approximated as a Gaussian distribution

$$P(n, \mu, \sigma^2) = \frac{1}{\sigma\sqrt{2\pi}} e^{-\frac{(n-\mu)^2}{2\sigma}},$$

where $\mu = \sigma^2 = <N>$. Fig A.1 shows the Gaussian curve for both standard

physics and new physics in case of $< N_B >= 53$ and $< N_S >= 51$. If there are no new physics, the observed events are expected to follow the left curve. But if there are new physics the observed events are expect to follow the right curve instead. The overlapped area of two curves indicates the probability that the new physics that we observed comes from the fluctuation of standard physics. This area, κ, can be calculated numerically from

$$
\begin{aligned}
\kappa &= \frac{1}{\sqrt{2\pi}\sigma_2} \int_{-\infty}^{\sigma_1\sigma_2} \exp\left[-\frac{(x-\sigma_2^2)^2}{2\sigma_2^2}\right] dx + \frac{1}{\sqrt{2\pi}\sigma_1} \int_{\sigma_1\sigma_2}^{\infty} \exp\left[-\frac{(x-\sigma_1^2)^2}{2\sigma_1^2}\right] dx \\
&= \frac{1}{\sqrt{2\pi}} \left[\int_{-\infty}^{\sigma_1-\sigma_2} \exp\left[-\frac{y^2}{2}\right] dy + \int_{\sigma_2-\sigma_1}^{\infty} \exp\left[-\frac{y^2}{2}\right] dy\right] \\
&= 1 - erf\left(\frac{\sigma_2-\sigma_1}{\sqrt{2}}\right).
\end{aligned}
$$

In this case, $\sigma_1 = \sqrt{< N_B >}$ and $\sigma_2 = \sqrt{< N_B > + < N_S >}$.

Here, The quality factor are defined as $Q = 2(\sigma_2-\sigma_1) = \sqrt{< N_S > + < N_B >} - \sqrt{N_B}$, which plays the direct roles to this probability. The Q-factor can be written in term of significance S_1 and S_2 as $Q = 2\frac{S_1 S_2}{S_1+S_2}$. For $N_B \gg N_S$, $Q \approx S_1 \approx S_2$. For $S_1 = 5$ according to 5σ confidence, $Q \approx 5$ corresponding to the probability $\kappa = 1.2\%$.
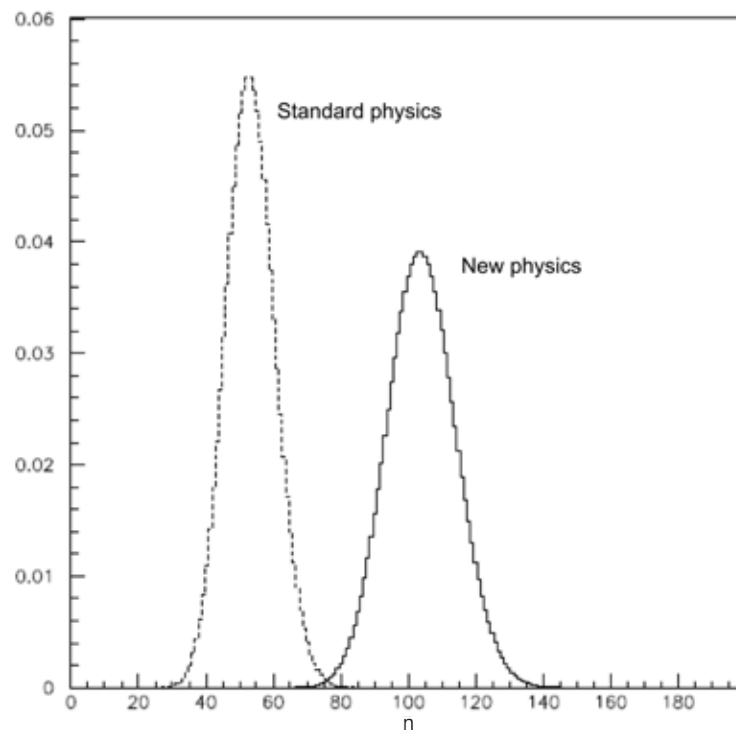
Figure A.1: The Gaussian distribution function for standard physics and new physics in the case of $< N_B >= 53$ and $< N_S >= 51$.

Vitae

Mr. Nattawit Chaiworawitsakul was born on 13 December 1988 and received his Bachelor's degree in physics from Mahidol University in 2010. He has studied general relativity, quantum field theory, and elementary particle physics for his Master's degree. His research interest is in particle physics, particularly in the area of supersymmetry search.

Presentations

1. Characteristics of Supersymmetry Signal and Background at $\sqrt{s} = 7\,\text{TeV}$ in the Fully Hadronic Channel: Siam Physics Congress 2014, Rajamangala University of Technology Isan, Nakhon Ratchasima, Thailand, 26-29 March 2014.

International Schools

1. The 2$^{\text{nd}}$ Particle Physics School in South-East Asia 2012, Universitas Gadjah Mada, Yogyakarta, Indonesia, 16-22 September 2012.

2. The 2$^{\text{nd}}$ CERN School Thailand 2012, Suranaree University of Technology, Nakhon Ratchasima, Thailand, 23 April - 5 May 2012.

3. The 3$^{\text{rd}}$ School of Physics at LHC, Quynhon University, Quy Nhon, Vietnam, 12-17 December 2011.

4. The 1$^{\text{st}}$ CERN School Thailand 2010, Chulalongkorn University, Bangkok, Thailand, 4-13 October 2010.